5-2005

# The Discrete-Dipole Approximation and Its Applications to Surface-Enhanced Raman Scattering

Albert Eugene DePrince III
*University of Tennessee - Knoxville*

# The Discrete-Dipole Approximation and Its Applications to Surface-Enhanced Raman Scattering

**Eugene DePrince**
**Department of Chemistry**
**University of Tennessee, Knoxville**

**Senior Honors Thesis**
**May 2005**

# 1. Introduction:

Vibrational spectroscopy is a very important tool by which scientists may identify molecular species and quantify their concentration in a sample. Infrared (IR) spectroscopy concerns itself with the absorption of infrared light by a molecule at discrete energies, leading to vibrational excitation of the molecule. Each IR-active mode of a molecule absorbs light at a characteristic energy, making the assignment of vibrational modes useful in the determination of unknown molecular species. There are several problems with IR spectroscopy which render it insufficient to classify all vibrational modes of all molecules. First, only those vibrational modes which result in a change in the dipole moment of the molecule can absorb IR radiation. Second, $H_2O$ absorbs infrared radiation to a great degree in large portions of the IR spectrum. Figure 1 depicts the IR absorption spectrum for $H_2O$ [12].

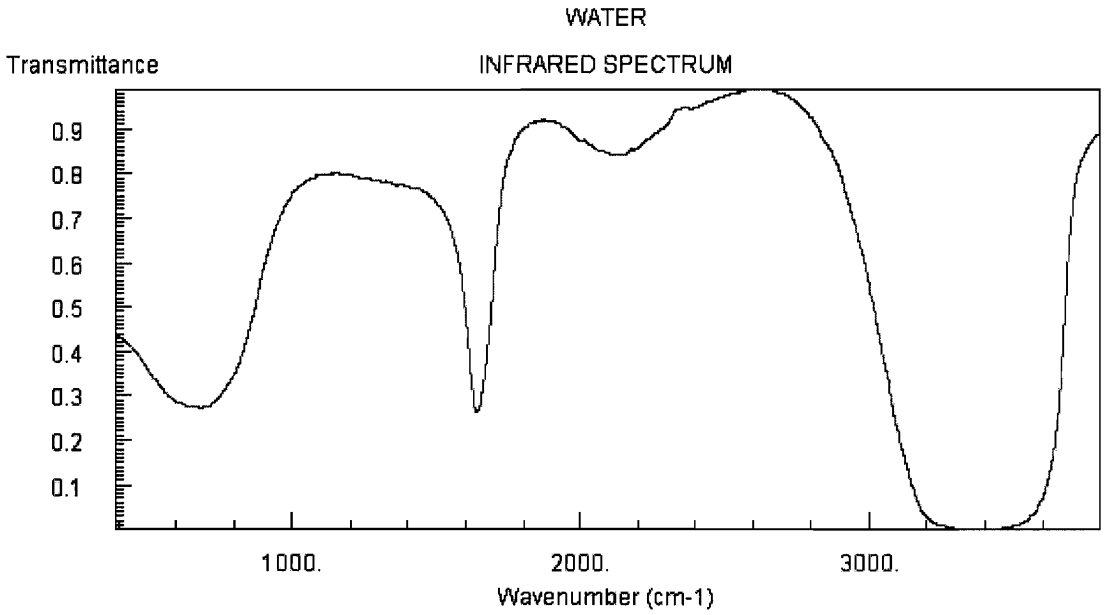


Figure 1. IR absorption spectrum for water.

Obviously there will be great difficulty in qualifying and quantifying species that absorb radiation in regions dominated by $H_2O$ absorption; the most troublesome regions are below 1000 and above 3000 wavenumbers.

These problems may be circumvented by the use of Raman scattering in place of IR spectroscopy. Raman scattering occurs when incident light of arbitrary radiation strikes a molecule, raises it to a virtual excited state, and scatters off it at a different energy. This change

in energy corresponds to a vibrational excitation in the molecule. The vibrational modes which may be viewed via Raman spectroscopy must result in a change in the polarizability of a molecule. Between IR- and Raman-active vibrational modes, nearly all the vibrational modes of a molecule may be observed.

Raman spectroscopy also has the distinct advantage over IR spectroscopy that it may be carried out in aqueous media. Aqueous measurements are possible because the intensities of Raman scattering signals of water are far more moderate than IR signals. The IR absorption cross section of liquid $H_2O$ is $1.4 \times 10^{-19}$ $cm^2$/molecule [17] in the range of 2800-3800 $cm^{-1}$. This value is an averaged value over this particular region. The Raman scattering cross section for liquid water in the 3000-3750 $cm^{-1}$ range is $1.02 \times 10^{-28}$ $cm^2$/molecule [13]. The scattering cross section for liquid water in this region is much smaller than the IR absorption cross section, meaning that Raman scattering is a useful phenomenon that may be used to identify unknown molecules in biological or other aqueous samples.

In the gas phase, Raman scattering is an extremely rare event. The majority of scattering that occurs is inelastic Rayleigh scattering, in which the energy of the scattered photon does not change during the collision with a molecule. For this reason, Raman spectroscopy was not a valuable tool until the 1970s. In 1977, Albrecht and Creighton [14] found that pyridine adsorbed onto roughened silver electrodes led to anomalously large Raman scattering signals. This phenomenon has been traced to the adsorption of the analyte molecules onto small (on the order of 100 nm in diameter) spheres of silver or gold. These spheres have become known as nanoparticles, and the phenomenon has been termed surface-enhanced Raman scattering (SERS). The nanoparticles, through a mechanism which is not yet completely understood, magnify the electric field associated with incident laser light in their vicinity. These local increases in electric field are believed to be responsible for the dramatic increase in Raman signal observed. Observed surface-enhanced Raman scattering signal can be as large as a factor of $10^6$ times gas-phase Raman scattering signal; increases in signal also scale roughly with the fourth power of the relative increase in electric field magnitude. For these reasons, a computer code to simulate the response of such nanoparticles to incident laser radiation and its associated electric field would be beneficial to our understanding and harnessing of SERS.

There exists such a method to determine local electric field enhancements due to the presence of nanoparticles. We may monitor such enhancements due to the presence of simple

systems such as isolated nanoparticles, as well as due to more complicated arrays of nanoparticles with varying geometries and interparticle distances. This method was developed by Purcell and Pennypacker [1] in the 1970s to investigate the scattering of light by interstellar material. This method, the discrete-dipole approximation (DDA), can determine scattering, absorption, and extinction efficiencies for light scattering off spheres and ellipsoids of arbitrary size and dielectric constant. It may also be used to determine interparticle electromagnetic enhancements for arbitrarily shaped nanoparticles as mentioned above. Purcell and Pennypacker compared DDA-calculated efficiencies to those obtained from Mie theory, which, in its simplest terms, is the solution to Maxwell's equations that govern the propagation of electromagnetic radiation in the vicinity of a small spherical particle.

In this thesis, we use the DDA to determine the optical properties of a variety of nanoparticles. We do extensive checks on the accuracy of the DDA with respect to existing analytical and numerical methods. We also begin an investigation of the optical properties of simple arrays of nanoparticles, with the hopes of comparing our computational results to experimental results. The remainder of the thesis is organized as follows. Section 2 describes the DDA approach in more detail and outlines three computational approaches used as a check on the accuracy of our DDA results. Section 3 presents the results of our DDA simulations. Section 4 gives some brief concluding remarks and points out prospects for future work.

## 2. Methods:

### *2.1 The DDA*

The simplest geometric form that nanoparticles may assume is spherical. Our study therefore begins with a single spherical nanoparticle. The DDA models this nanoparticle by first subdividing it into a contiguous collection of polarizable elements situated on a cubic lattice. A sphere is therefore approximated by a collection of cubic units. Figure 2 illustrates the approximated sphere as a collection of polarizable units. Each point in the figure is located at the center of the cubic unit.

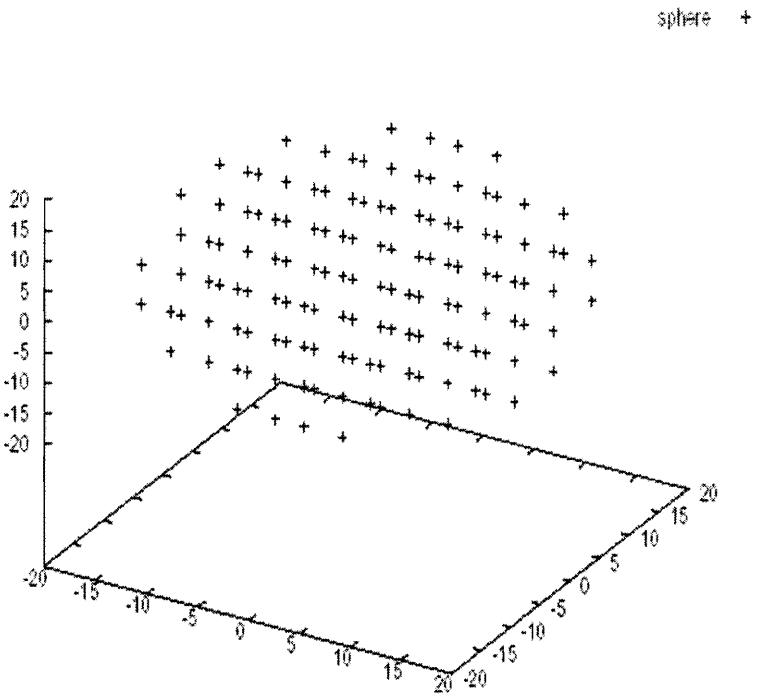


Figure 2. Sphere Approximated on Cubic Lattice, units in Bohr.

We are not limited to spheres in our analysis. Virtually any shaped nanoparticle is feasible for simulation; we limit ourselves, however, to simple geometric shapes. Illustrated in figure 3 is another simple solid studied here, the prolate spheroid.

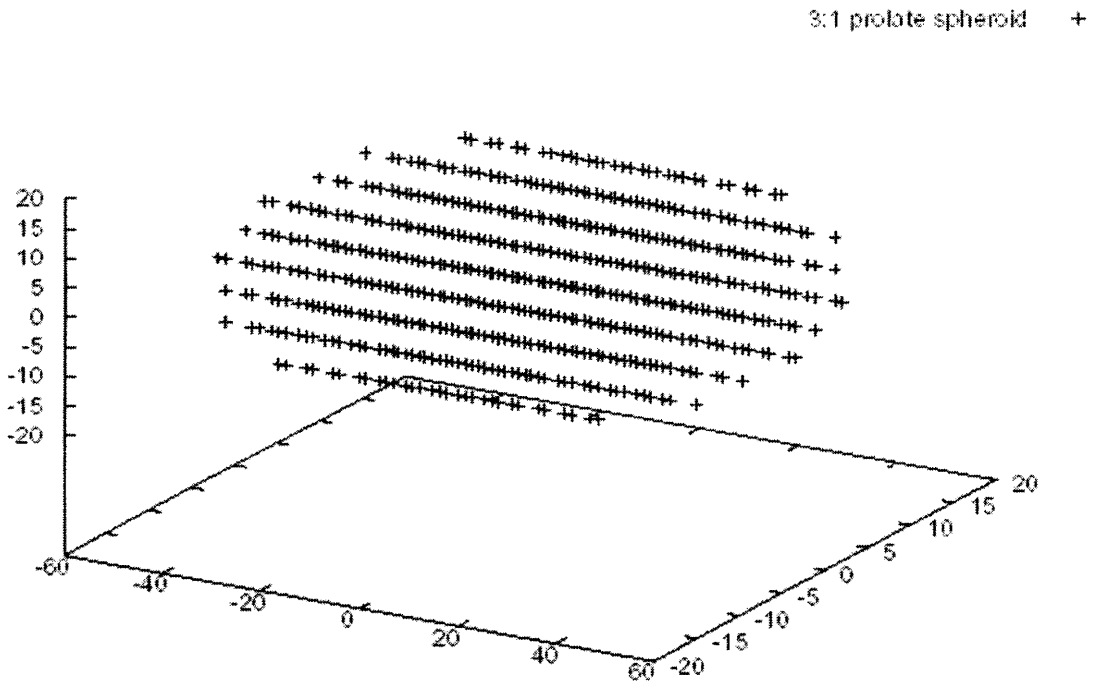


Figure 3. Prolate Spheroid Approximated on Cubic Lattice, units in Bohr.

In mathematical terms, the DDA considers the response of each of the polarizable elements under consideration to the electric field associated with an incident electromagnetic wave. Dipoles are induced at each element by the incident wave, and each of these induced dipoles generates an associated electric field that may affect all other dipoles. Through successive iterations, a self-consistent set of dipoles is eventually obtained that approaches the real-world polarization for the simulated nanoparticle in the limit of infinite subdivision of the block.

First, the incident electric field is considered. We assume that the incident radiation is traveling in the $x$-direction, with the electric field polarized in the $z$-direction. The magnitude of this electric field at the $i^{th}$ dipole is given,

$$\mathbf{E}_i = E_o \mathbf{1}_z \exp[i(\omega \cdot t - kx_i)], \tag{2.1.1}$$

where $E_o$ is the magnitude of the electric field, $\mathbf{1}_z$ is the $z$ unit-vector, $\omega$ is the circular frequency of the radiation, and $k$ is the wave vector for the light,

$$k = \frac{2\pi}{\lambda}, \tag{2.1.2}$$

where $\lambda$ is the wavelength of the light. Equation 2.1.1 is simplified by assuming that time, $t$, is equal to zero in all simulations. An initial dipole moment is then determined at each dipole, according to the electric field at that point and the polarizability $\alpha_i$ of that element:

$$\mathbf{P}_i = \alpha_i \mathbf{E}_i . \tag{2.1.3}$$

We discuss below approaches for relating $\alpha_i$ to the dielectric constant of the material.

This initial guess is then used to determine a new electric field felt at each point, which is the sum of the incident electric field and that contributed by each induced dipole. This idea is expressed mathematically as

$$\mathbf{E}_i = E_o \mathbf{1}_z \exp(ikx_i) + \sum_{j \neq i} \frac{\exp(ikr_{ij})}{r_{ij}^3} \left[ k^2 (\mathbf{r}_{ij} \times \mathbf{P}_j) \times \mathbf{r}_{ij} + \frac{(1 - ikr_{ij})}{r_{ij}^2} (3\mathbf{P}_j \bullet \mathbf{r}_{ij} \mathbf{r}_{ij} - r_{ij}^2 \mathbf{P}_j) \right], \quad (2.1.4)$$

where $\mathbf{r}_{ij}$ is the distance vector between two interacting dipoles and $r_{ij}$ is the magnitude of that distance vector. Equation 2.1.4 is separable into six inhomogenous equations, three describing the $x$, $y$, and $z$ real components of the electric field and three describing the imaginary components. Equations 2.1.4 and 2.1.3 are computed iteratively until the difference between values obtained at successive iterations are sufficiently small.

The bulk dielectric constant for the material is used to determine the polarizability of each element on the lattice. The simplest definition of polarizability is drawn from the Clausius-Mossotti (CM) relation [16],

$$\varepsilon - 1 = \frac{4\pi N\alpha}{1 - (4/3)N\alpha}, \quad (2.1.5)$$

where $N$ is the density of polarizable elements, $\varepsilon$ is the complex bulk dielectric constant (the square of the refractive index) for the material, and $\alpha$ is the polarizability of each element. The CM relation provides an approximation for the bulk dielectric constant that approaches the true value in the limit of infinite density.

The Clausius-Mossotti relation assumes that each element is situated on an infinite lattice of identical elements [16]. In the case of any finite object, however, this is not the case. The polarizabilities of elements in an object's outer layers will differ from those of elements toward the center. As we move toward the center of the object, the polarizability approaches the limit of the Clausius-Mossotti relation. A more rigorous definition of the polarizabity of each cubic element could therefore be utilized to obtain higher degrees of accuracy in the DDA calculations [11]. According to this more rigorous definition, the polarizability of element $i$ is determined by

$$\alpha_i = \frac{\varepsilon - 1}{4\pi} \Lambda_i^{-1} d^3, \quad (2.1.6)$$

where $\Lambda_i$ is defined as the local field tensor at the position of element *i*. This tensor is a function of the depolarization tensor for the material under investigation, which is determined by both the dielectric constant of the material and the shape of the object simulated (i.e. sphere, ellipse, etc.). We study objects such as spheres and spheroids that have a constant depolarization tensor, dependent solely upon the shape of the object. These constants are well described in the literature [5], [10].

We may verify numerically that the corrected polarizabilities for elements in a finite solid approach the Clausius-Mossotti value as their surroundings approach the limit of the infinite lattice. In other words, we may observe that, as we move toward the center of our solid, in this particular case a sphere, the polarizability tensor approaches the Clausius-Mossotti value. Figure 4 shows this for a spherical silver nanoparticle of radius 100 nm, approximated by 739 cubic elements.

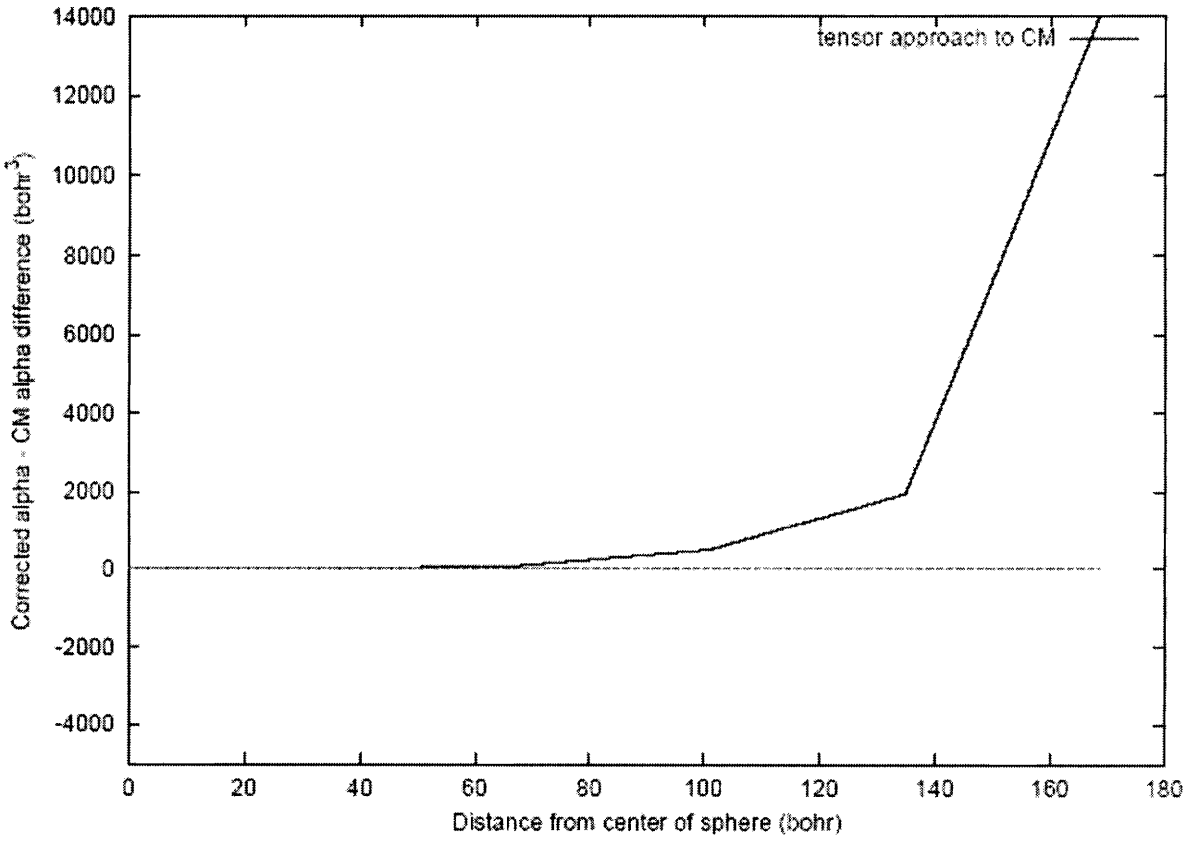


Figure 4. Approach of Corrected Polarizabilities to CM value.

While the mathematics of the original DDA paper provide a framework for the calculations, the iterative method put forth by Purcell and Pennypacker lacks sufficient stability to converge under all circumstances, despite their efforts to introduce techniques to improve convergence. For this reason, many researchers have been modifying and creating new iterative methods for DDA applications. One such method that has proven stable enough to converge in virtually all circumstances is that of B.T. Draine [2]. Each individual unit's influence on every other unit may be contained in one large $3M$ x $3M$ complex influence matrix, $\widetilde{\mathbf{A}}$, where $M$ is the number of polarizable units or dipoles involved in the simulation. The incident electric field at the position of each polarizable unit is stored in a single $3M$-dimensional complex vector, $\widetilde{\mathbf{E}}$. The result of this consolidation is to reduce the $6M$ inhomogeneous equations of Purcell and Pennypacker that account for the real and imaginary components of the 3-dimensional vectors describing the electric field at each dipole to a single matrix equation.[1]

$$\widetilde{\mathbf{A}}\widetilde{\mathbf{P}} = \widetilde{\mathbf{E}} \tag{2.1.7}$$

Their solution is obtained by a conjugate gradient algorithm described by Petravic and Kuo-Petravic [8]; this algorithm avoids direct inversion of the influence matrix to solve for the dipoles of each individual unit, contained in the $3M$-dimensional complex vector $\widetilde{\mathbf{P}}$. The iterative method put forth is not especially fast, but it proves extremely stable.

Another important consideration for the utilization of iterative techniques for matrix inversion is memory allocation. Direct inversion of a matrix requires that the entire matrix be held in RAM during the entire calculation. Our influence matrices sometimes contain on the order of $10^7$ matrix elements; obviously, using computationally appropriate levels of precision for each floating point number stored, we may easily surpass the memory capacities of our machines. Iterative methods have the distinct advantage that the entire matrix designated for inversion is not required to be held in RAM at all times. Matrix elements may be read from the hard drive as they are needed. In the next subsection, we give an outline of the conjugate gradient algorithm for solving equation 2.1.7.

[1] Draine also modified the Clausius-Mossotti relation to account for a "radiative reaction" [2].

## *2.2 Conjugate Gradient Algorithm*

The solution to the linear system described in equation 2.1.7 is obtained through what Petravic and Kuo-Petravic [8] term the conjugate gradient algorithm. This iterative method for solving complex linear systems avoids computationally expensive direct inversion of the complex influence matrix $\widetilde{A}$. The algorithm for computing the solution vector $\widetilde{P}$ is as follows. We start with an initial guess at the solution vector; the algorithm is then started with,

$$z \equiv \widetilde{A}^{\mp}\widetilde{E}, \tag{2.2.1}$$

$$g_0 = z - \widetilde{A}^{\mp}\widetilde{A}\widetilde{P}_0, \tag{2.2.2}$$

$$p_0 = g_0, \tag{2.2.3}$$

$$w_0 = \widetilde{A}\widetilde{P}_0, \tag{2.2.4}$$

$$v_0 = \widetilde{A}p_0, \tag{2.2.5}$$

where $\widetilde{A}^{\mp}$ is defined as the Hermitian conjugate of the influence matrix, $\widetilde{A}$,

$$(\widetilde{A}^{\mp})_{jk} = (\widetilde{A}_{kj})^{*}. \tag{2.2.6}$$

The computational costs of this start-up series of equations may be minimized by taking an initial guess of $\widetilde{P}_0 = 0$. The iterative scheme continues over several iterations, $i = 0, 1, 2, 3, \ldots$

$$\alpha_i = \frac{\langle g_i \mid g_i \rangle}{\langle v_i \mid v_i \rangle}, \tag{2.2.7}$$

$$\widetilde{P}_{i+1} = \widetilde{P}_i + \alpha_i p_i, \tag{2.2.8}$$

$$w_{i+1} = w_i + \alpha_i v_i, \tag{2.2.9}$$

$$g_{i+1} = z - \widetilde{A}^{\mp} w_{i+1}, \tag{2.2.10}$$

$$\beta_i = \frac{\langle g_{i+1} \mid g_{i+1} \rangle}{\langle g_i \mid g_i \rangle}, \tag{2.2.11}$$

$$p_{i+1} = g_{i+1} + \beta_i p_i, \tag{2.2.12}$$

$$v_{i+1} = \widetilde{A} g_{i+1} + \beta_i v_i. \tag{2.2.13}$$

This algorithm is such that the values for $w_i$ and $v_i$ will tend to drift from their true values, as defined in equations 2.2.14 and 2.2.15,

$$v_i \equiv \widetilde{A} p_i, \tag{2.2.14}$$

$$w_i \equiv \widetilde{A} \widetilde{P}_i. \tag{2.2.15}$$

The alternate definitions presented in equations 2.2.9 and 2.2.13 are in place to reduce computational costs associated with the full matrix-vector multiplications found in equations 2.2.14 and 2.2.15. The effect of the values of $v$ and $w$ straying from their exact values is reduced by computing the definitions outlined in equations 2.2.14 and 2.2.15 every $10^{th}$ iteration. This scheme is continued until the change in the norm of the $z$-component of the solution vector $\widetilde{P}$ falls within a predefined tolerance. We have found empirically that the proper tolerance to balance accuracy and time requirements is $1 \times 10^{-4}$,

$$\Delta \| \widetilde{P}_z \| \leq 10^{-4}. \tag{2.2.16}$$

We may use DDA-based simulations to compute many properties of a nanoparticle in an oscillating (or static) electric field. We may compute the scattering, absorption, and extinction cross sections for nanoparticles in oscillating electric fields. For particles in static fields, we may compute the particle's polarization, or dipole per unit volume. For both oscillating and static electric fields, we may compute local electric field enhancement and perturbations in electric potential near the surface of the nanoparticle.

We are also very interested in changes in the accuracy of the DDA simulations that result from the adoption of either equation 2.1.5 or 2.1.6 as the definition of polarizability. We therefore need a reference against which we may compare the results of our DDA simulations. For spherical nanoparticles, we may use Mie theory to asses the accuracy of DDA-based predictions of the scattering, absorption, and extinction cross sections, and of the local field

enhancement in the vicinity of the nanoparticles. For a spherical nanoparticle in a static electric field, we may compute the expected polarization of the nanoparticle from the sphere's depolarization tensor for comparison with DDA-simulated polarizations. For spheroidal particles in a static field, we may compute the electric potential near the surface of the particle for comparison with DDA-derived electric potential. In the next three subsections, we discuss each of these methods for generating reference results against which we can compare our DDA results.

## *2.3 Mie Theory*

Mie theory [15], developed originally to understand scattering of light in gold colloidal solutions (commonly found in stained glass at that time), is a theory that utilizes Maxwell's equations that govern the propagation of electromagnetic radiation to study the scattering of light by small spheres with radius on the order of the wavelength of light scattered. For our purposes, Mie theory is quite useful in determining the accuracy of the DDA for such scattering problems. We limit ourselves in this section to spherical objects.

Mie theory allows us to calculate analytically the absorption, scattering, and extinction cross sections for a particular scattering event. Put simply, a cross section is a measure of the strength of a particular interaction of light with the sphere. The cross section has units of area; a unitless quantity called the efficiency may be obtained by dividing a cross section by the geometric cross-section of the sphere, $\pi R^2$.

We begin our analysis by determining Mie scattering coefficients, $a_n$ and $b_n$, as per the derivation found in [5]. We first define

$$\psi_n(\rho) = \rho j_n(\rho), \qquad \xi_n(\rho) = \rho h_n^{(1)}(\rho), \tag{2.3.1}$$

$$h_n^{(1)}(\rho) = j_n(\rho) - iy_n(\rho). \tag{2.3.2}$$

where $\rho$ is a dummy variable and $j_n$ and $h_n^{(1)}$ are Ricatti-Bessel functions. We define a parameter, $x$, based upon the radius to wavelength ratio of our system,

$$x = ka = \frac{2\pi a}{\lambda}, \tag{2.3.3}$$

where $a$ is the radius of the sphere and $\lambda$ is the wavelength of the incident radiation. The relative refractive index of the system, $m$, must be defined as,

$$m = \frac{N_1}{N_0}, \tag{2.3.4}$$

where $N_1$ and $N_0$ are the refractive indices of the particle and the medium in which it is located, respectively. This ratio simply becomes equal to $N_1$ in our system, as the particle is found in vacuum ($N_0 = 1$). We now have sufficient information to determine our scattering coefficients [5]:

$$a_n = \frac{m\psi_n(mx)\psi_n'(x) - \psi_n(x)\psi_n'(mx)}{m\psi_n(mx)\xi_n'(x) - \xi_n(x)\psi_n'(mx)} \tag{2.3.5}$$

$$b_n = \frac{\psi_n(mx)\psi_n'(x) - m\psi_n(x)\psi_n'(mx)}{\psi_n(mx)\xi_n'(x) - m\xi_n(x)\psi_n'(mx)} \tag{2.2.6}$$

The scattering and extinction cross-sections are then determined [5]:

$$C_{scat} = \frac{2\pi}{k^2}\sum_{n=1}^{\infty}(2n+1)\left(|a_n|^2 + |b_n|^2\right), \tag{2.3.7}$$

$$C_{ext} = \frac{2\pi}{k^2}\sum_{n=1}^{\infty}(2n+1)\,\mathrm{Re}\{a_n + b_n\}, \tag{2.3.8}$$

where $k$ is the wavevector of the incident radiation. The cross sections are now normalized to the system under investigation as mentioned above.

$$Q_{scat} = \frac{C_{scat}}{\pi R_e^2}, \qquad Q_{ext} = \frac{C_{ext}}{\pi R_e^2} \tag{2.3.9}$$

$$Q_{abs} = Q_{ext} - Q_{scat}. \tag{2.3.10}$$

As Mie theory limits its descriptions to spheres, in order to determine the accuracy of DDA-generated efficiencies, we must simulate spheres. We may approximate a sphere on a cubic lattice and define a parameter called the equivalent radius of the sphere.

$$R_e = (3Md^3 / 4\pi)^{1/3}, \tag{2.3.11}$$

where d is defined as the spacing between each cubic element. The equivalent radius is simply the radius of a true sphere that has a volume equivalent to that contained in our approximate sphere consisting of $M$ cubic elements at a density of $N$. This radius is that used in the equations of Mie theory. It is a necessary parameter in determining the accuracy of DDA predictions.

Scattering, absorption, and extinction efficiencies are determined numerically [2] for DDA-simulated spheres. The extinction and absorption cross sections may be determined from the incident electric field and the self-consistent set of dipoles determined by the iterative process previously mentioned,

$$C_{ext} = \frac{4\pi k}{|\mathbf{E}_i|^2} \mathrm{Im}(\mathbf{E}_i^* \bullet \mathbf{P}_i), \tag{2.3.12}$$

$$C_{abs} = \frac{4\pi k}{|\mathbf{E}_i|^2} \sum_{i=1}^{M} \left\{ \mathrm{Im}[\mathbf{P}_i \bullet (\alpha^{-1})^* \mathbf{P}_i^*] - \frac{2}{3} k^3 \mathbf{P}_i \bullet \mathbf{P}_i^* \right\}, \tag{2.2.13}$$

where $\mathbf{E}_i$ is the incident electric field at position $i$, as defined in equation 2.1.3. The efficiencies are determined as before by dividing these cross sections by the geometric cross sections,

$$Q_{abs} = \frac{C_{abs}}{\pi R^2}, \qquad Q_{ext} = \frac{C_{ext}}{\pi R^2}. \tag{2.3.14}$$

It should be noted that the $R$ in the DDA geometric cross section differs from the equivalent radius used in the Mie theory calculations. $R$ here is the true radius of the sphere under investigation. The scattering efficiency may be determined from the difference between the extinction and absorption efficiencies.

$$Q_{scat} = Q_{ext} - Q_{abs} . \tag{2.3.15}$$

The level of subdivision of the sphere (the density $N$ of polarizable elements in the approximated sphere) is directly related to the accuracy of the DDA with respect to Mie theory solutions. The finer the discretization of the sphere, the greater the time and memory requirements for the simulation become. These requirements increase roughly with $27M^3$, where $M$ is the number of polarizable elements to be simulated.

## *2.4 Static Field Calculations*

For simple geometric solids such as spheres, there are compact expressions describing theoretical magnitudes of induced dipoles, in the limit of infinite wavelength of light. Put simply, we may predict the average dipole magnitude the DDA should produce when a nanoparticle is placed in a static electric field. For a sphere, this theoretical dipole magnitude in the limit of infinite subdivision of the solid is given by

$$P_\infty = (3d^3 / 4\pi)(\varepsilon - 1)(\varepsilon + 2)^{-1} . \tag{2.4.1}$$

where $d$ is the length of one of the cubic elements comprising the solid. DDA-generated dipole magnitudes were obtained by

$$P = \sqrt{|\mathbf{P}_x|^2 + |\mathbf{P}_y|^2 + |\mathbf{P}_z|^2} , \tag{2.4.2}$$

where $|\mathbf{P}|$ denotes the complex absolute value of that term.

In a real solid with a diagonal depolarization tensor (like the spheres and spheroids studied here), dipoles should always align with the electric field of the incident radiation. As yet

another measure of the accuracy of the DDA, one could monitor the angle between the dipoles generated by the DDA and the direction along which the electric field of incident radiation is polarized ($z$). This angle, $\theta$ is given by

$$\theta = \cos^{-1}\left(\frac{|\mathbf{P}_z|}{P}\right). \tag{2.4.3}$$

Deviations from the ideal value $\theta = 0$ arise as a result of the rough approximation of a sphere used in the DDA. We find that the dipoles at or near the corner dipoles of the approximated sphere deviate slightly from alignment with the external electric field. Theoretically, this effect could be lessened by finer subdivision in the sphere.

## *2.5 Poisson Equation*

Our final check on the validity of DDA obtained solutions to the scattering problem is another analytic method that yields exact solutions. We can solve Poisson's equation to determine the electric potential both inside and outside a dielectric spheroid positioned in a static electric field. The equations associated with this method may be found, for those interested, in [10]. This method, in conjunction with Mie theory, allows us to determine the capability of the DDA to model both spheres and spheroids of arbitrary dielectric constant.

We begin this particular analysis with the definition for the surface of an ellipsoid,

$$\frac{z^2}{a^2}+\frac{x^2}{b^2}+\frac{y^2}{c^2}=1. \tag{2.5.1}$$

A family of ellipsoidal surfaces may be described through the introduction of a parameter, $\xi$, which has units of length$^2$:

$$\frac{z^2}{a^2+\xi}+\frac{x^2}{b^2+\xi}+\frac{y^2}{c^2+\xi}=1. \tag{2.5.2}$$

This ellipsoid is placed at the origin in a uniform electric field ($k$=0), $\mathbf{E}_0 = E_{0,z}\hat{\mathbf{z}}$ oriented along the $z$ axis. This field is generated by the potential $\Phi_0 = -zE_{0,z}$. In the calculations presented below, we set $E_{0,z} = 1$ to compute relative potentials and field enhancements. We may define the potential inside the ellipsoid as,

$$\Phi_{in} = -\frac{zE_{0,z}}{1+abc(\varepsilon_1-\varepsilon_0)A_z/(2\varepsilon_0)}, \tag{2.5.3}$$

where $\varepsilon_1$ and $\varepsilon_0$ are the inductive capacities of the ellipsoidal material and the medium in which it is situated, respectively, and

$$A_z = \int_0^\infty \frac{du}{(u+c^2)^{3/2}(u+a^2)^{1/2}(u+b^2)^{1/2}}. \tag{2.5.4}$$

$A_z$ is a factor of units length$^{-3}$ which depends only the relative magnitudes of the three semi-axes of the ellipsoid. The electric field within the ellipsoid is then defined as

$$E_{in,z} = -\frac{\partial\Phi_{in}}{dz} = E_{0,z}\times\frac{1}{1+abc(\varepsilon_1-\varepsilon_0)A_z/(2\varepsilon_0)}, \tag{2.5.5}$$

and satisfies

$$E_{in,z} = E_{0,z} - L_z P_z. \tag{2.5.6}$$

The induced polarization within the ellipsoid whose $z$-component is given by $P_z$ reduces the effect of the applied field inside the ellipsoid. The field within the ellipsoid therefore carries the term $L_z$, the depolarization factor along the $z$-axis. The induced polarization is defined by

$$\mathbf{P} = (\varepsilon_1-\varepsilon_0)\mathbf{E}_{in}, \tag{2.5.7}$$

and its $z$-component is therefore defined as

$$P_z = (\varepsilon_1 - \varepsilon_0)E_{in,z} \tag{2.5.8}$$

We insert equation 2.5.8 into equation 2.5.6 and obtain

$$E_{0,z} = E_{in,z}\left[1 + L_z(\varepsilon_1 - \varepsilon_0)\right], \tag{2.5.9}$$

$$1 + L_z(\varepsilon_1 - \varepsilon_0) = 1 + abc(\varepsilon_1 - \varepsilon_0)A_z/(2\varepsilon_0), \tag{2.5.10}$$

and, solving for $L_z$,

$$L_z = \frac{abcA_z}{2\varepsilon_0}. \tag{2.5.11}$$

We may simplify by observing that, in atomic units, $\varepsilon_0 = 1/4\pi$ so we get

$$L_z = 2\pi abcA_z \tag{2.5.12}$$

Similarly, we find that

$$L_y = 2\pi abcA_y \qquad \text{and} \qquad L_x = 2\pi abcA_x \tag{2.5.13}$$

where,

$$A_x = \int_0^\infty \frac{du}{(u+c^2)^{1/2}(u+a^2)^{3/2}(u+b^2)^{1/2}} \text{ and } A_y = \int_0^\infty \frac{du}{(u+c^2)^{1/2}(u+a^2)^{1/2}(u+b^2)^{3/2}} \tag{2.5.14}$$

The factors *a*, *b*, and *c* describe the *x*, *y*, and *z* semi-axes of the ellipsoid in question. We may simplify all the above equations by limiting our investigation to the case of prolate spheroids, in which $c > a = b$. With this simplification, it is possible to evaluate the integral in equation 2.5.4 analytically, giving

$$A_z = \int_0^\infty \frac{du}{(u+c^2)^{3/2}(u+a^2)} = \frac{1}{c^3 e^3}\left(-2e + \ln\frac{1+e}{1-e}\right), \tag{2.5.15}$$

where $e$ is defined as the eccentricity,

$$e = \sqrt{1 - a^2/c^2}\ . \tag{2.5.16}$$

In addition, the terms $A_x$ and $A_y$ have been simplified,

$$A_x + A_y + A_z = \frac{2}{a^2 c}, \tag{2.5.17}$$

$$A_x = A_y = \frac{1}{a^2 c} - \frac{A_z}{2}. \tag{2.5.17}$$

We may now define the dielectric constant as the relative permittivity of the ellipsoid, $\kappa_1 = \varepsilon_1/\varepsilon_0$, and the electric potential outside of the prolate spheroid as

$$\Phi_{out} = \Phi_0\left[1 + \frac{1-\kappa_1}{1+(a^2 c A_z/2)(\kappa_1 - 1)}\frac{a^2 c}{2}\int_\xi^\infty \frac{du}{(u+c^2)^{3/2}(u+a^2)}\right]. \tag{2.5.18}$$

The integral in equation 2.5.18 is evaluated numerically to determine perturbations in the electric potential about the prolate spheroid. We compare these results to those of the DDA as yet another measure of the accuracy of the DDA.

## 3. Results:

### *3.1 Comparisons to Mie Theory*

In order to determine if our own DDA program was functioning correctly, a plot of exact Mie solutions for scattering, absorption, and extinction efficiencies as a function of the parameter

$x$ defined in equation 2.3.3 was produced. The corresponding points generated by the DDA program were compared to this plot, as shown in Figure 5. The definition of polarizablity utilized in these simulations was that of the CM relation (equation 2.1.5).

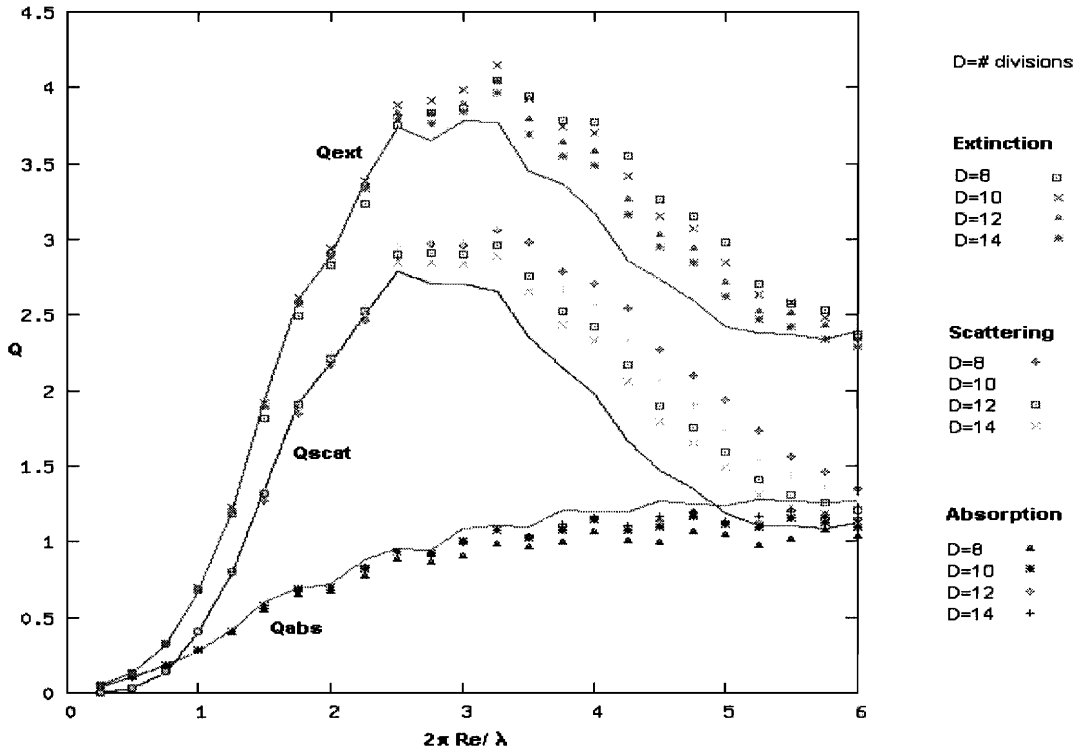


Figure 5. Comparison of efficiencies obtained from DDA to those of Mie theory as a function of $2\pi R_e/\lambda$. Solid lines represent exact Mie Theory solutions. $\varepsilon = 2.88 + 0.34i$

As the level of subdivision of the spheres in the DDA program was increased, the DDA-generated points approach the exact Mie solutions, presumably, in the limit as the level of subdivision approaches infinity. This trend is analogous to that of the Clausius-Mossotti relation; as the sphere's discretization becomes finer, its behavior under light approaches that of the corresponding real world object. This preliminary trial utilizes the dielectric constant of dirty ice ($\varepsilon = 2.88 + 0.34i$) for easy comparison to plots generated in references [1] and [2]. One other reference dielectric constant was utilized to determine the accuracy of the DDA program. The material simulated had a dielectric of $\varepsilon = -7 + 24i$. This material was simulated by Purcell and Pennypacker; our use of the material is for the sake of completeness. A plot of efficiencies as a function of the term $x$ is shown in figure 6.

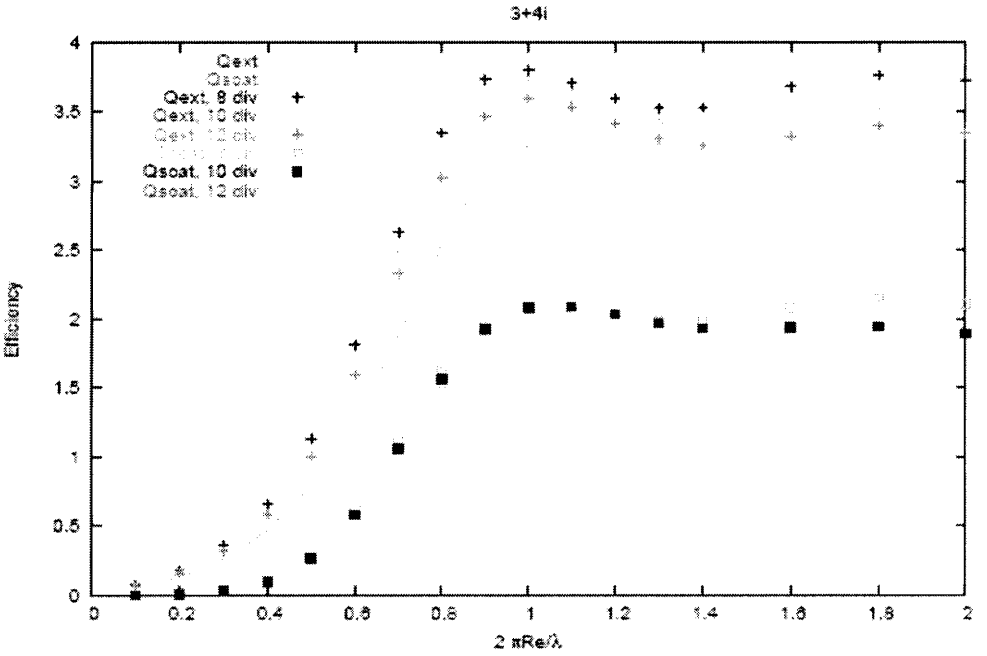


Figure 6. Comparison of efficiencies obtained from DDA to those of Mie theory as a function of $2\pi R_e/\lambda$. Solid lines represent exact Mie Theory solutions. $\varepsilon$ = -7+24i ($m$=3+4i)

Preliminary results suggest that our DDA code can simulate light interactions with a single sphere of dirty ice or the material with $\varepsilon$ = -7 + 24i to an acceptable degree of accuracy, based upon comparisons of DDA and Mie theory efficiencies. Subdivision beyond what is shown will give greater accuracy, but with increased time and memory requirements. The cost of further subdivision may outweigh any benefits in terms of accuracy.

Surface-enhancement of Raman signal is most often accomplished with nanoparticles composed of silver or gold. We therefore attempted to create a plot of efficiencies of laser light interactions with silver nanoparticles. Figure 7 contains the same information as figures 5 and 6 for silver. From the figure, it is clearly apparent that a greater degree of subdivision is necessary for accurate DDA-generated values for silver. At this point, however, memory restrictions prevent us from simulating spheres at finer levels of discretization.

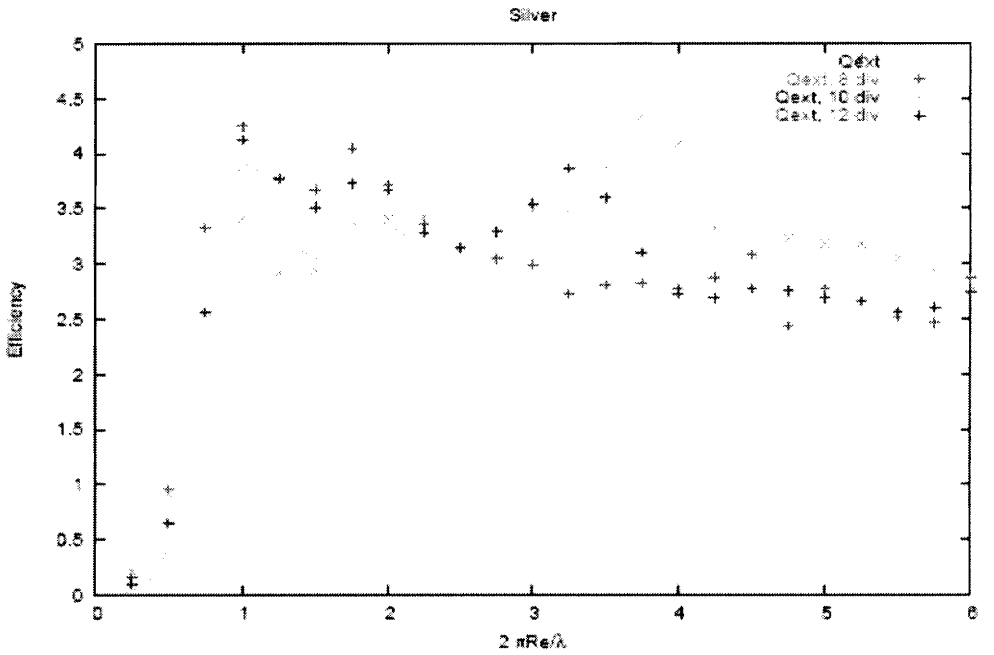


Figure 7. Comparison of extinction efficiencies obtained from DDA to those of Mie theory as a function of $2\pi R_e/\lambda$. The solid line represents the exact Mie Theory solution. $\varepsilon = -15.88 + 1.05i$ [6].

## *3.2 Resonance Peaks*

To understand the transition between highly accurate simulations of dirty-ice to those of low accuracy of silver, we devised a scheme to 'ramp' up the imaginary portion of the refractive index of our simulated material. Our scheme is based upon a parameter, β, arbitrarily increased from a value of 0 to 30,

$$m = c(1 + \beta i) \tag{3.2.1}$$

where $m$ is the refractive index of the material and $c$ is an arbitrary constant. For our particular simulations, we set $c = 0.134547$, corresponding to the real component of the refractive index of silver under 632.8 nm radiation. Arbitrarily increasing β leads to an increasingly negative real component of the dielectric constant for the material. Figure 8 illustrates DDA-generated efficiencies as compared to Mie theory values with increasing values of β; it should be noted that, in this scheme, the value β=30 produces a dielectric constant roughly equal to that of silver ($\varepsilon = -15.8754 + 1.0481$ i).

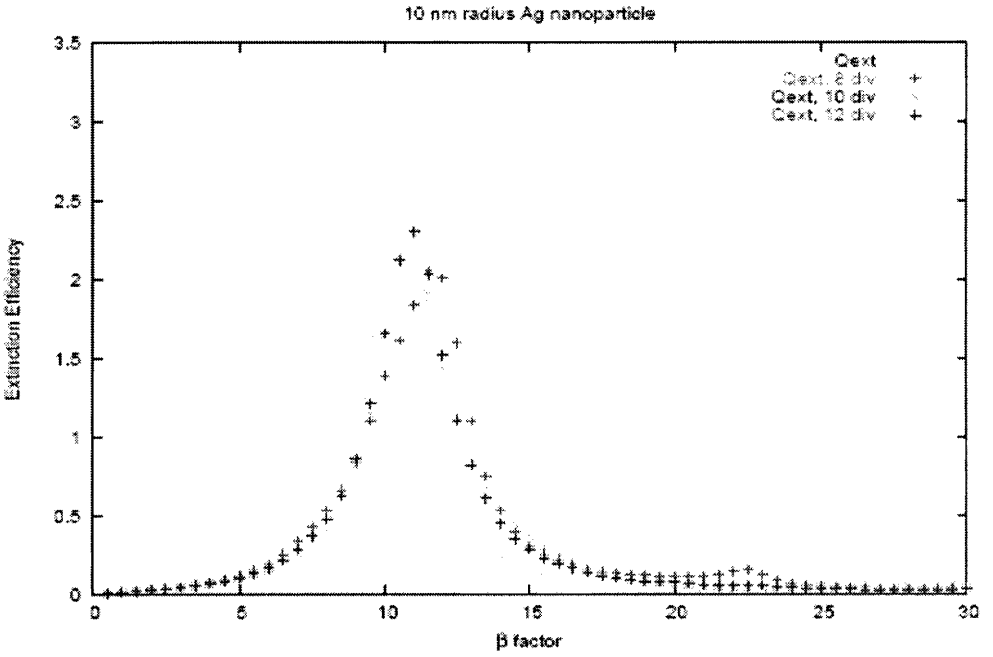
10 nm radius Ag nanoparticle
Qext
Qext, 8 div
Qext, 10 div
Qext, 12 div
Extinction Efficiency
β factor
0
0.5
1
1.5
2
2.5
3
3.5
0
5
10
15
20
25
30

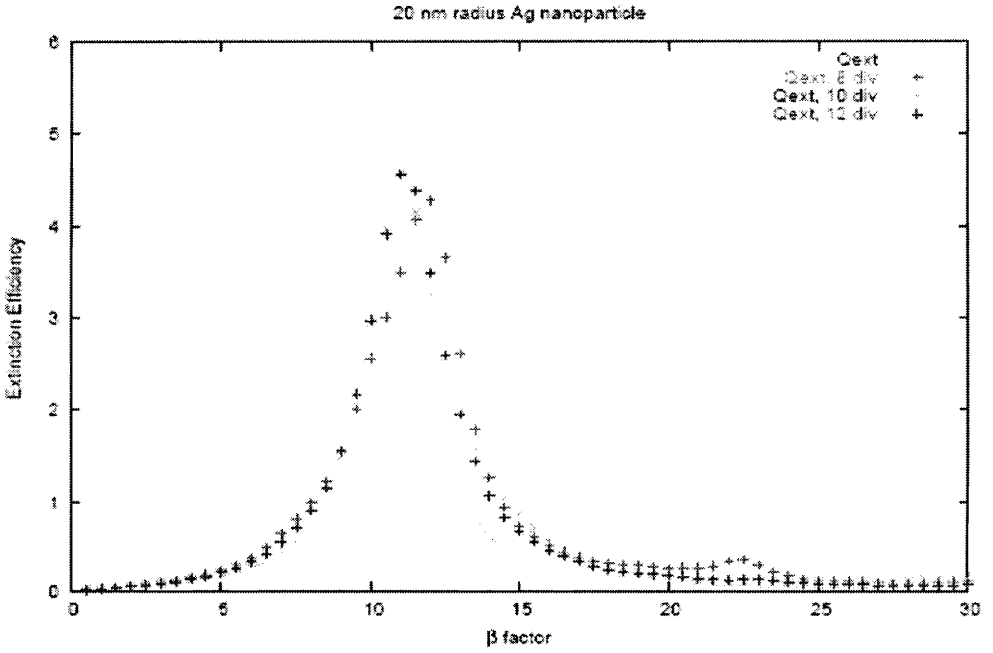
20 nm radius Ag nanoparticle
Qext
Qext, 8 div
Qext, 10 div
Qext, 12 div
Extinction Efficiency
β factor
0
1
2
3
4
5
6
0
5
10
15
20
25
30

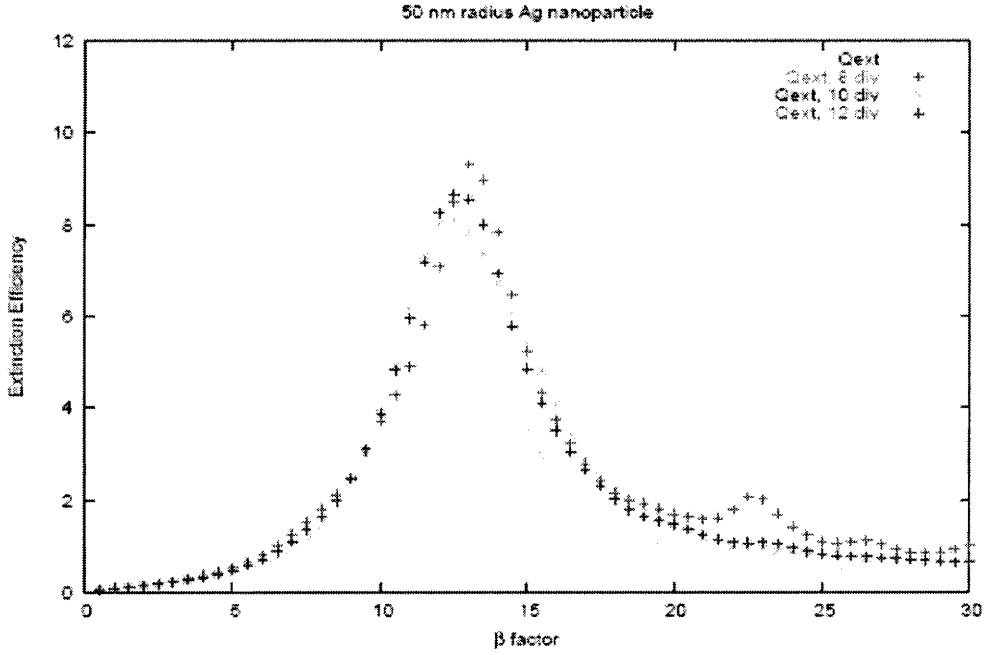
50 nm radius Ag nanoparticle
Qext
Qext, 8 div
Qext, 10 div
Qext, 12 div
Extinction Efficiency
β factor
0
2
4
6
8
10
12
0
5
10
15
20
25
30

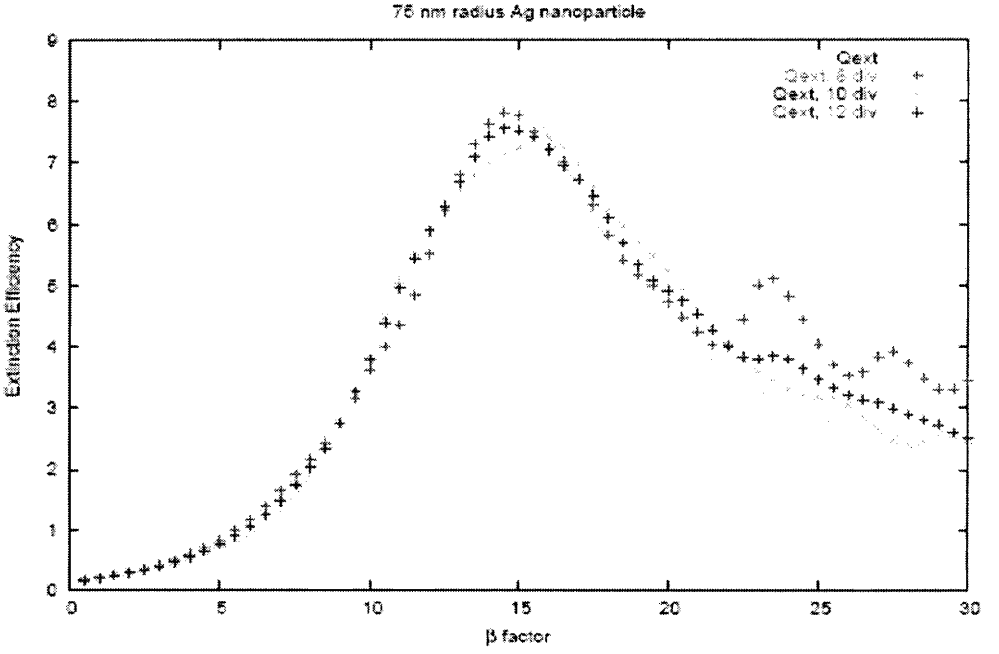
75 nm radius Ag nanoparticle
Qext
Qext, 8 div
Qext, 10 div
Qext, 12 div
Extinction Efficiency
β factor
0
1
2
3
4
5
6
7
8
9
0
5
10
15
20
25
30

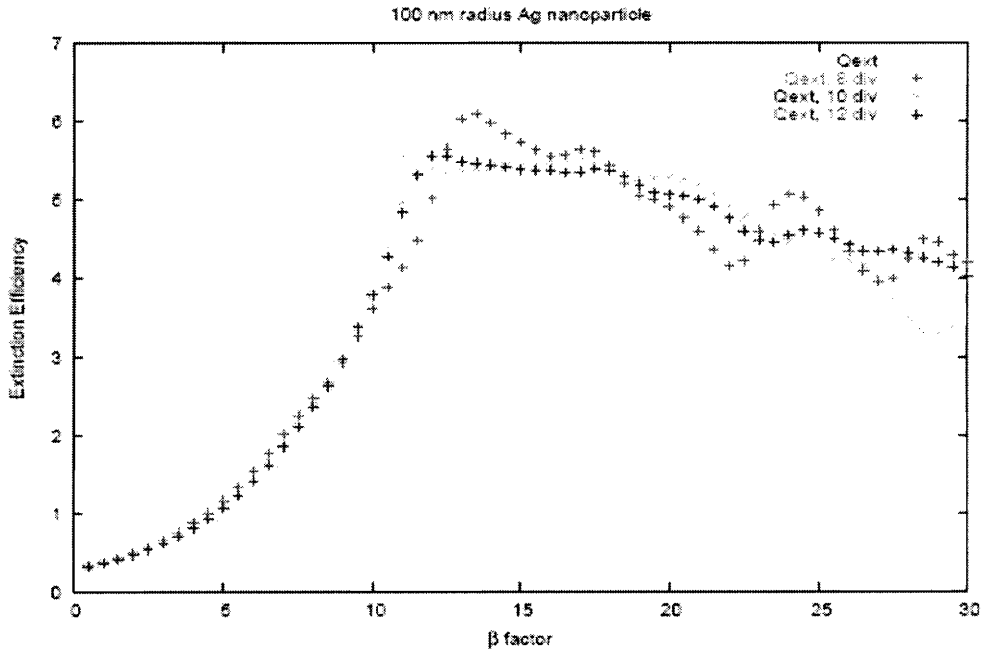


Figure 8. Spheres of varying size and dielectric constant under 632.8 nm radiation. m=0.134(1+βi)

Upon visual inspection of figure 8, one may notice that each plot contains a distinct peak around which the DDA has difficulty predicting efficiencies accurately. This peak is due to a resonance phenomenon that occurs at a wavelength characteristic of the material under investigation. The mathematics of light scattering is such that, for a particular dielectric constant, there exists a resonant wavelength that leads to very large cross sections. In the limit of $k$=0 (static electric field), the scattering cross section for a nanoparticle may be described by [5]:

$$Q_{sca} = \frac{8}{3} x^4 \left| \frac{\varepsilon - 1}{\varepsilon + 2} \right|^2 . \tag{3.2.2}$$

According to equation 3.2.2, we observe the resonant phenomenon when the real component of the dielectric constant is near -2. The above peaks, while in the finite $k$ regime, are the result of this basic phenomenon. In theory, for the purposes of SERS, the radius to wavelength ratio in shown in these plots should be chosen to maximize the scattering efficiency of the material. Although particles with this radius would have light scattering properties that would make them ideal SERS candidates, it is very difficult to simulate these near-resonance properties accurately using the DDA.

All DDA-generated efficiencies described to this point utilize the original CM (Eq. 2.1.5) definition for polarizability. We have had difficulty reproducing these simulations utilizing the volume-corrected version of the polarizability (Eq. 2.1.6). Despite these setbacks, we predict that the corrected version of polarizability will lead to significant improvements in DDA predictions of cross sections. These improvements should prove particularly important when simulating nanoparticles with near-resonance properties as described above.

## *3.3 Static Field Results*

The first dramatic evidence we obtained for the benefits of using the corrected polarizabilities for the finite solid has come in the comparison of the theoretical average dipole moment (Eq. 2.4.1) as compared to DDA-generated dipoles in the static field limit. Figure 9 shows the ratio of the DDA-generated dipoles for both the CM definition of polarizability and the corrected version to the theoretical value provided by equation 2.4.1. The material simulated is a silver sphere with a radius of 100 nm and $\varepsilon = -15.8754 + 1.0481\ i$. Should the DDA perform perfectly, we would observe a ratio of unity for all levels of subdivision.

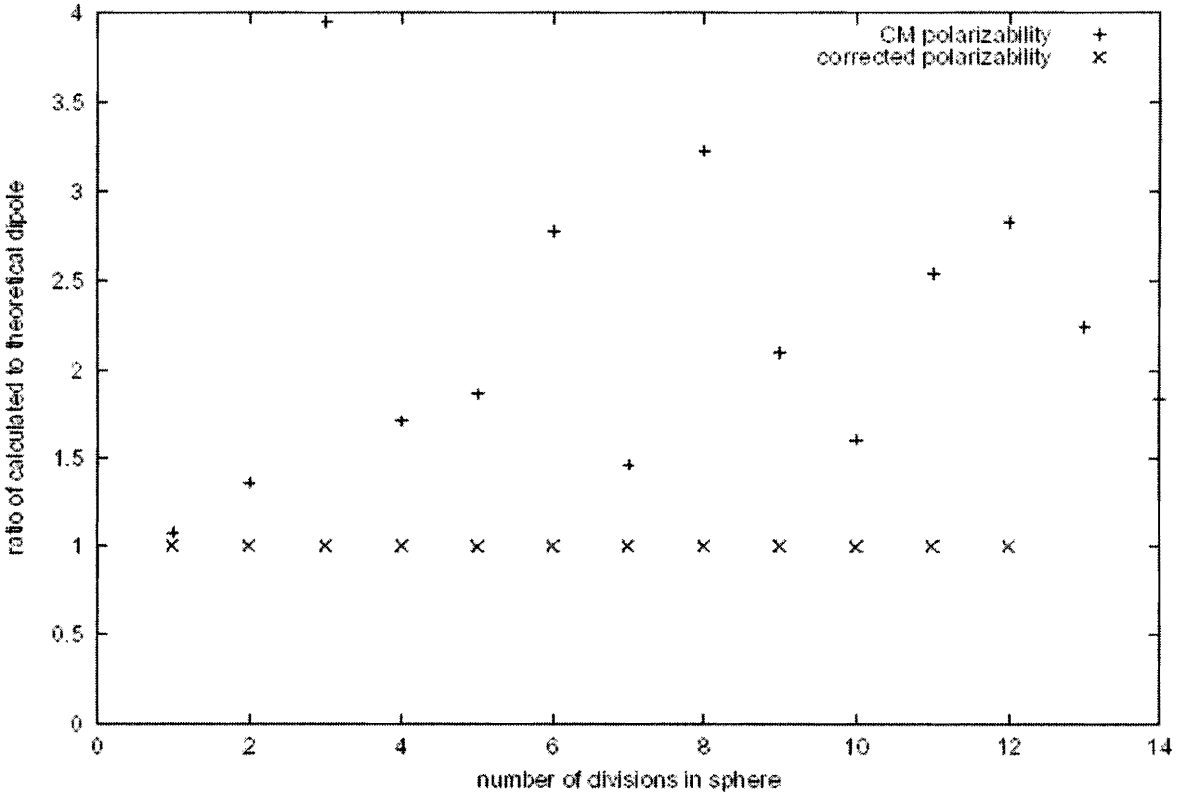


Figure 9. Static Field Dipoles Ratio (DDA/Theoretical)

Clearly, the corrected polarizabilities provide dramatic improvements to the performance of the DDA, in terms of accuracy.

### *3.4 Comparisons to Poisson's Equation*

The computed potential near the surface of a spheroidal nanoparticle situated in a static electric field as compared to the numerical solution to Poisson's equation has provided further evidence for the importance of the corrections to polarizability provided in equation 2.1.6. We have figures depicting the relative electric potential as perturbed by the presence of spheroidal nanoparticles, provided by both the DDA and numerical integration of Poisson's equation. Figure 10 depicts the effect of a silver prolate spheroidal nanoparticle with aspect ratio of 3:1 on the electric potential in its vicinity. Although the nanoparticle is situated in static electric field, it is given the dielectric constant corresponding to silver irradiated with $\lambda$=632.8 nanometer radiation.

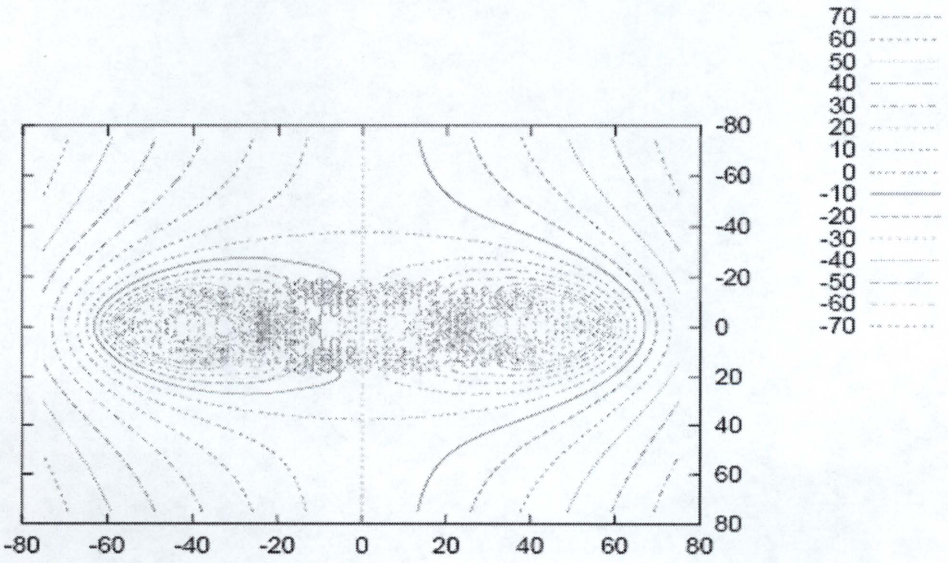


Figure 10. Contour plot of relative electric potential as perturbed by spheroidal nanoparticle ($\varepsilon$ = -15.88 + 1.05i). Corrected polarizabilities utilized.

The plots provided in this section were computed under static field conditions. We anticipate that, as wavelength of light is decreased to finite values, the differences between the CM and corrected polarizability versions of the DDA will become even more pronounced. Figure 10 was computed using corrected polarizabilities.

Figure 11 depicts potential around another silver 3:1 silver prolate nanoparticle; the difference here, though, is that the dielectric constant is that corresponding to silver at $\lambda = 494.2$ nanometers ($\varepsilon = -8.20 + 0.75\ i$). In a manner analogous to the resonant peaks observed in figure 8, prolate spheroids have characteristic dielectric constants and wavelengths at which light interactions are resonantly enhanced. These special dielectric constants are dependent upon the aspect ratio of the spheroid. We have seen at which wavelength a 3:1 prolate spheroid resonantly interacts. The special wavelengths for silver are $\lambda = 570.3$ nm and $\lambda = 648.3$ nm for 4:1 and 5:1 prolate spheroids, respectively. The length scale in these figures is Bohr, but it should be noted that the contours scale perfectly with size, meaning that the figures would be identical in any other length scale.

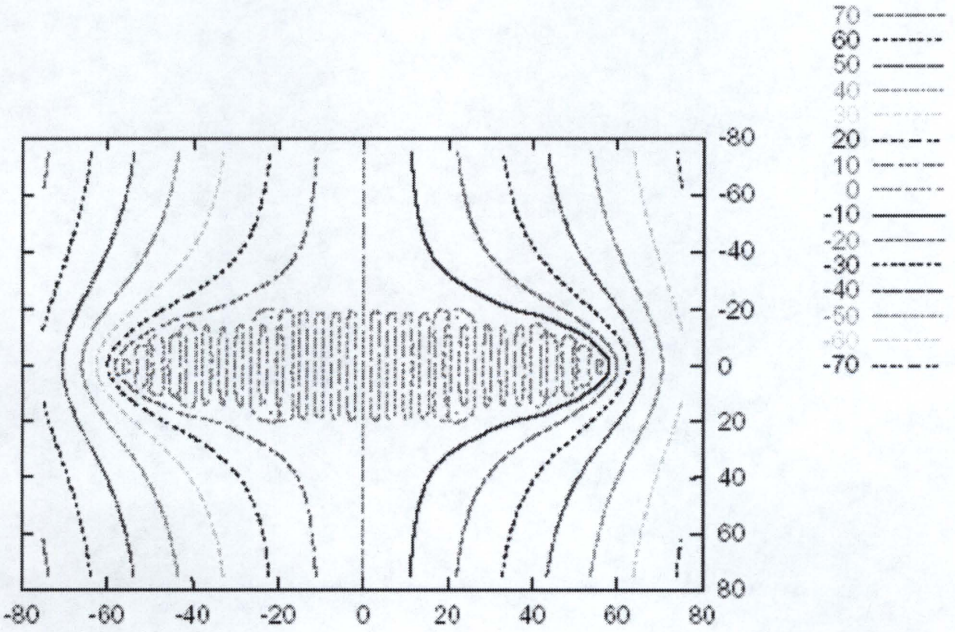

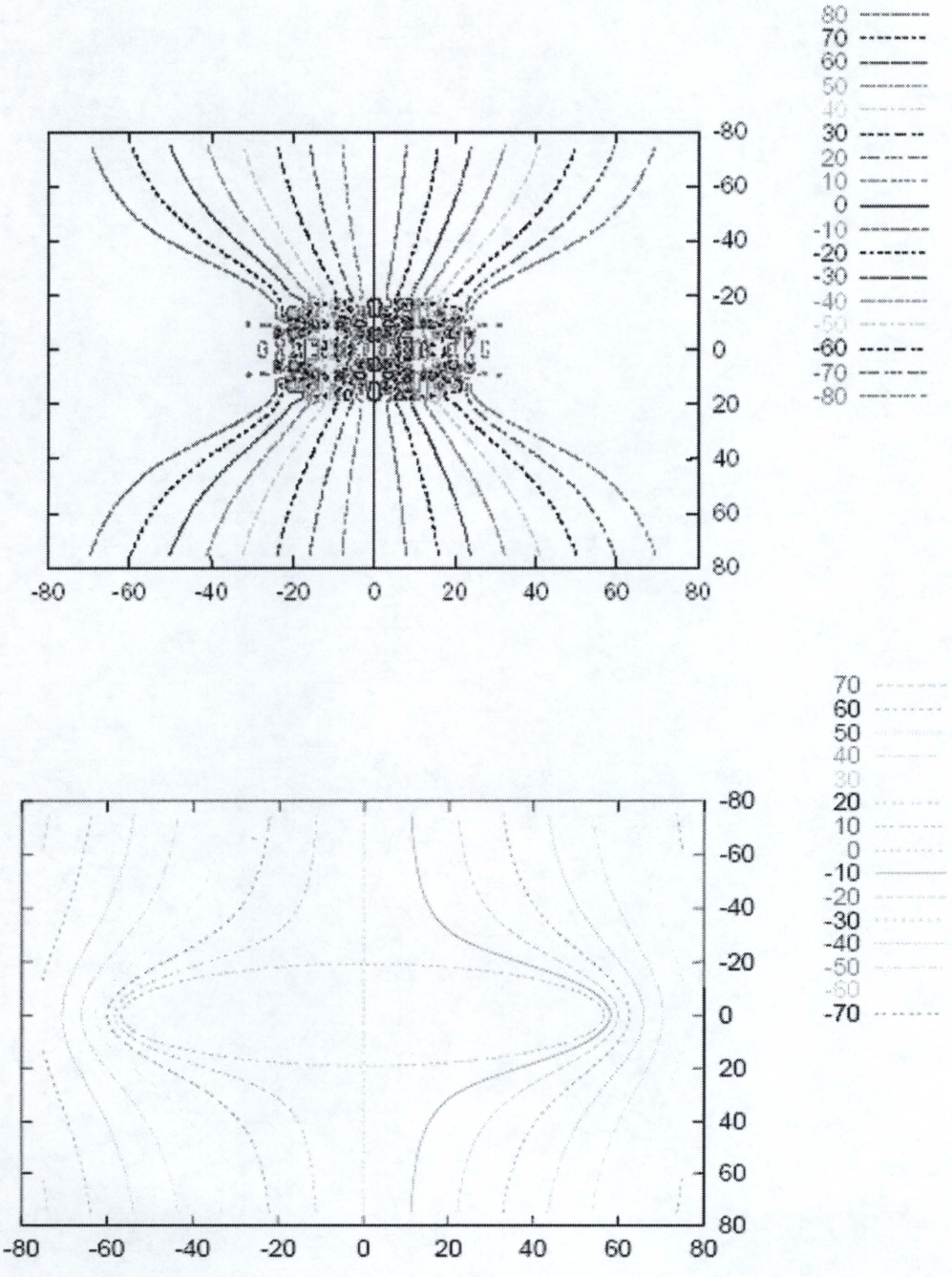


Figure 11. Electric potential about prolate spheroid. From top to bottom, figures generated using, corrected polarizabilites, CM polarizabilities, analytic solution.

One may notice from the above diagram that the uncorrected CM polarizabilities are insufficient to reproduce the numerical solution to Poisson's equation for the potential around our spheroid. The corrected polarizabilites provide far more accurate calculations. Noting this

difference is crucial when making other comparisons of the performance of the two versions of the DDA. As we will see below, distinctions between the two codes are more difficult.

It is postulated that the dramatic increases in Raman signal associated with SERS are due to local increases in electric field in the vicinity of nanoparticles. For this reason, a contour plot of the electric field around a silver 3:1 prolate spheroid ($\varepsilon = -8.20 + 0.75\ i$) in static field is included in figure 12.

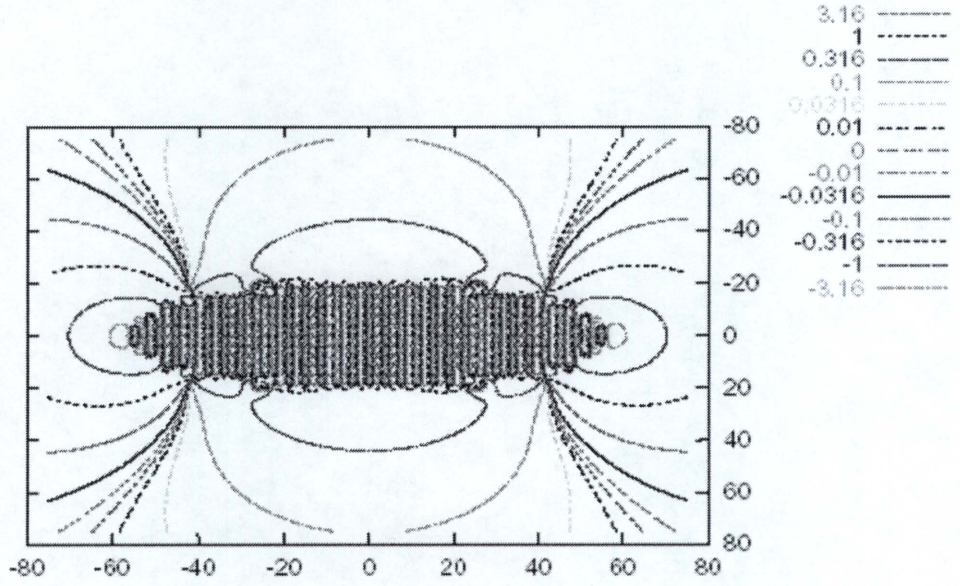


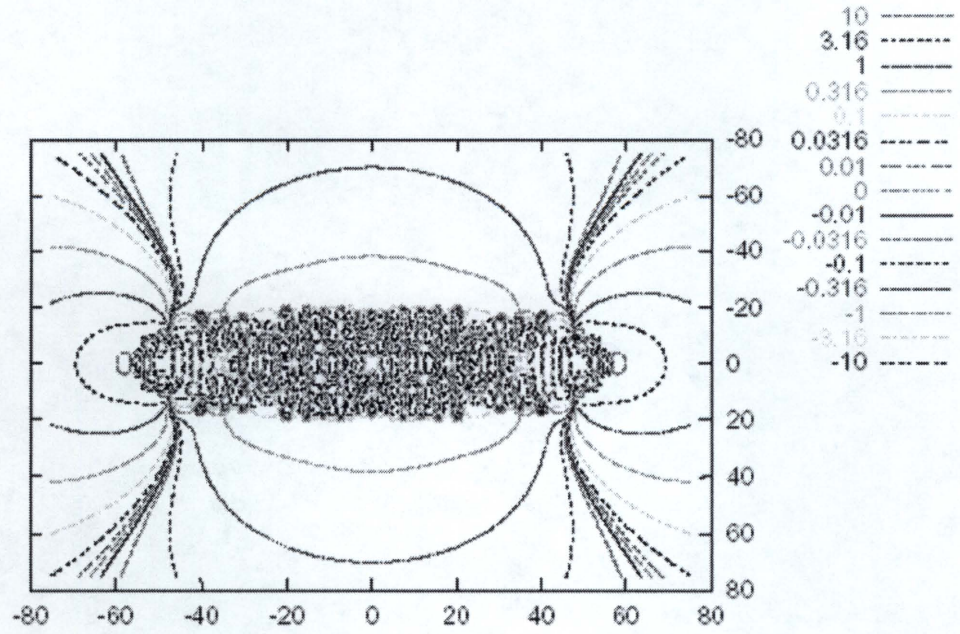

Figure 12. Electric field around prolate spheroid. From top to bottom, solutions generated utilizing corrected polarizabilities, uncorrected CM polarizabilities.

One notices that there are two 'hot spots' at the tips of the nanoparticle at which the field is highly perturbed. Should analyte molecules find themselves near those spots, they are likely candidates to participate in the surface-enhanced phenomenon. These hot spots differ roughly by a factor of three in the two figures. Recall that enhancements in Raman signal are proportional to the $4^{th}$ power of enhancements in electric field; this means that the difference of a factor of three in the electric field corresponds to a difference in predicted Raman scattering enhancement of a factor of eighty-one. Clearly, the corrections to the CM definition of polarizability play an important role in predicting SERS enhancements.

## *3.5 Applications of the DDA to SERS*

We are currently collaborating with members of the Sepaniak group at the University of Tennessee to provide predictions for Raman signal enhancement. Active sites for the surface-enhanced phenomenon are usually provided by colloidal solutions of metal or by vapor-depositing metals onto roughened glass microscope slides. Polymers onto which metals may be vapor deposited may also be pin-printed onto glass slides. The Sepaniak group is currently working to etch wells and patterns into silica via electron beam lithography, with the possibility of creating very precise and perhaps very elaborate patterns onto which silver may be deposited. The exact nature of this method is conducive to theoretical prediction and therefore a perfect real-world counterpart for testing the utility of our DDA methods.

We have run a simulation of the simplest array considered by the Sepaniak group. Two 10 x 50 x 100 $nm^3$ rectangular prisms are separated axially, either in the $y$- or $z$-directions. The laser wavelength in this simulation is 632.8 nm, the wavelength of a helium-neon (HeNe) laser. This geometry is particularly appealing because the Clausius-Mossotti relation utilizes a cubic lattice easily applied to rectangular prisms. At this wavelength, the bulk dielectric constant of silver is $\varepsilon = -15.88 + 1.05i$ [6]. Figure 13 depicts the relative enhancement of the $z$-component of the electric field vector as a function of distance between prism faces. The figure illustrates the instances in which the prisms are separated in both the $y$- and $z$-directions, instances in which the prisms are perpendicular or parallel to the plane of polarization of the light, respectively.

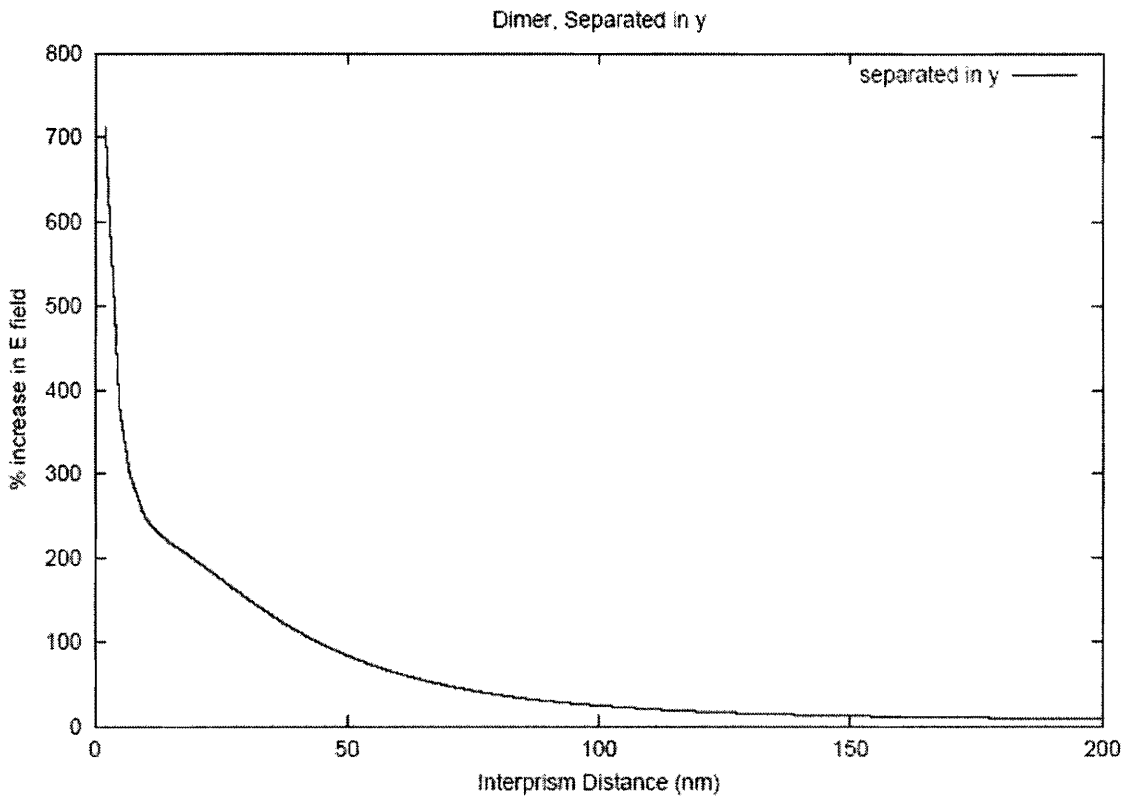


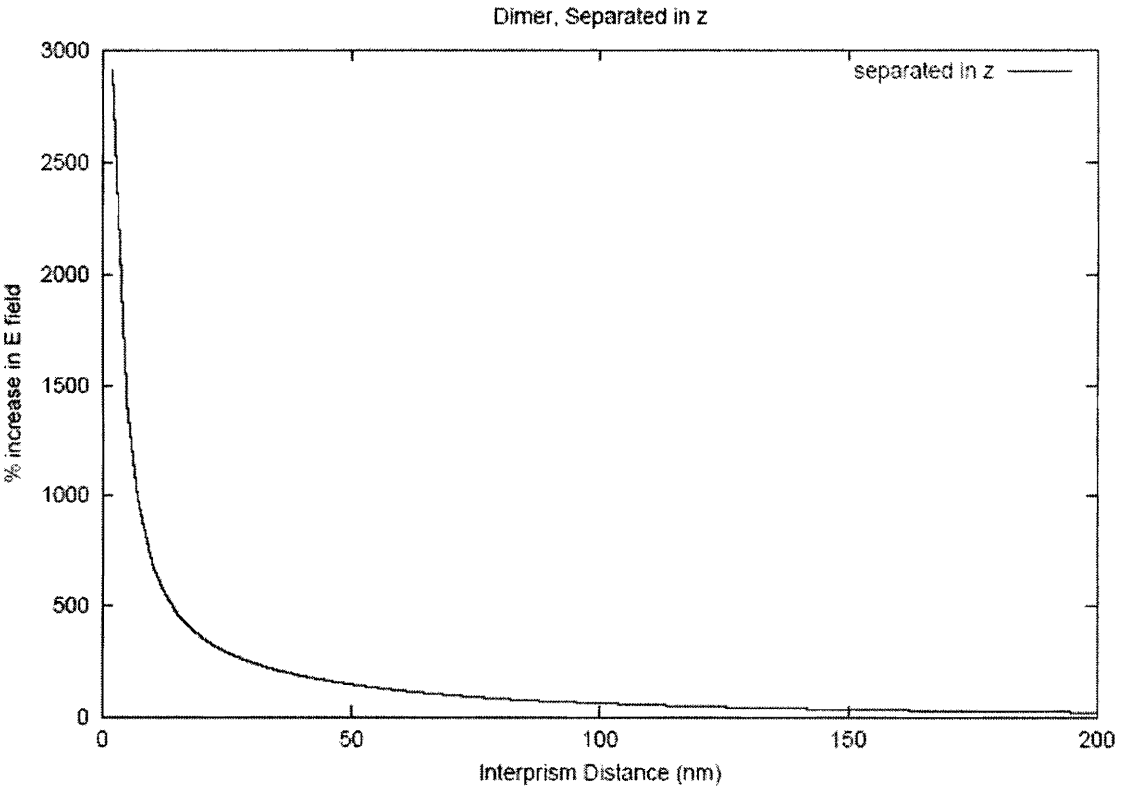


Figure 13. Increase in electric field magnitude as a function of the distance between prisms. $\varepsilon = -15.88 + 1.05i$.

Clearly we observe greater enhancements when the prisms are separated in the *z*-direction. In order to compare these results with experimental work, the enhancements in the two orientations would be averaged, thus accounting for non-polarized laser light utilized in the laboratory. One may also note the kink in the curve corresponding to separation in the *y*-direction. We attribute this behavior to the fact that, as interprism distances become comparable to inter-dipole distances within individual nanoparticles, the DDA has some difficulty distinguishing between the two nanoparticles. We have yet to compare these results with experimental observation.

Despite the relatively poor accuracy of the DDA solutions compared to those of Mie theory presented in Figure 7, this simulation may contain some realistic qualities. The density of the cubes that make up these particular rectangular prisms is far greater than that of the cubes composing the spheres used to generate Figure 7. If we expand the prisms so that they have similar dimensions to the spheres, while keeping the cube density constant, we can see that the prism simulation in effect utilizes a degree of subdivision well beyond our memory limitations for the sphere simulations. As stated above, as the level of subdivision increases, the results of the discrete dipole approximation approach those of Mie theory and reality.

We have recently compared our simulations of simple arrays of nanoparticles with experimental data collected by Marco De Jesus of the Sepaniak group at the University of Tennessee. Three simple patterns of nanoparticles were investigated. The first was a four-nanoparticle square arrangement of rectangular prisms with dimensions 10 x 175 x 175 $nm^3$. The prisms were separated in the *y*-*z* plane with a distance of 175 nm between faces. From this point on, this arrangement will be referred to as 'quadramer-big.' The next array was similar to the first; it was composed of four rectangular prismatic nanoparticles with dimenstions 10 x 100 x 100 $nm^3$. They were separated in the *y*-*z* plane with a distance between faces of 50 nm. This array will be referred to as 'quadramer-small.' The last array was a hexamer of equilateral triangles arranged in a hexagon, separated in the *y*-*z* plane. The base of each triangular prism was 50 nm. The height of the prism (in the *x*-direction) was 10 nm. The inter-facial distance of the array was 50 nm.

As we have demonstrated the benefits of the utilization of corrections to the polarization, we have used only the corrected versions of polarizability for these simulations. The

depolarization tensors used for each array were equivalent to those appropriate for modeling spherical nanoparticles. Future work in this area will include the numerical determination of the depolarization tensors corresponding to rectangular and triangular prisms.

Figures 14 depicts the complex absolute value of the increases in electric field about these three nanoparticles with initial electric field magnitude $E_0 = 1$.

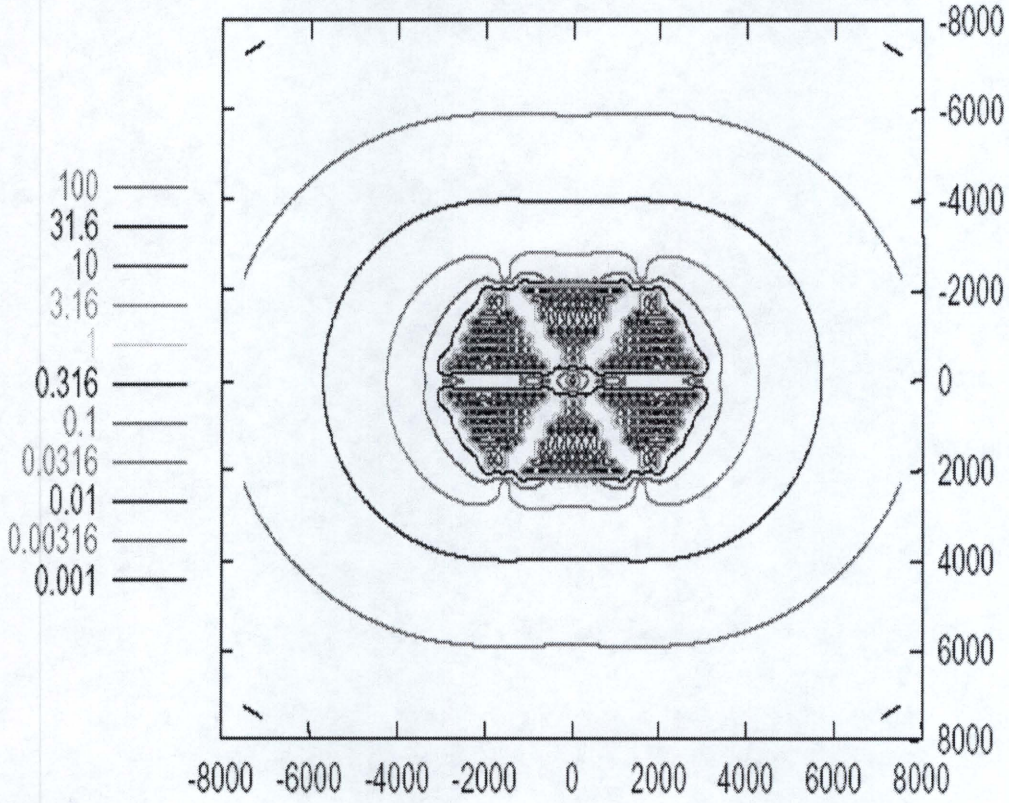

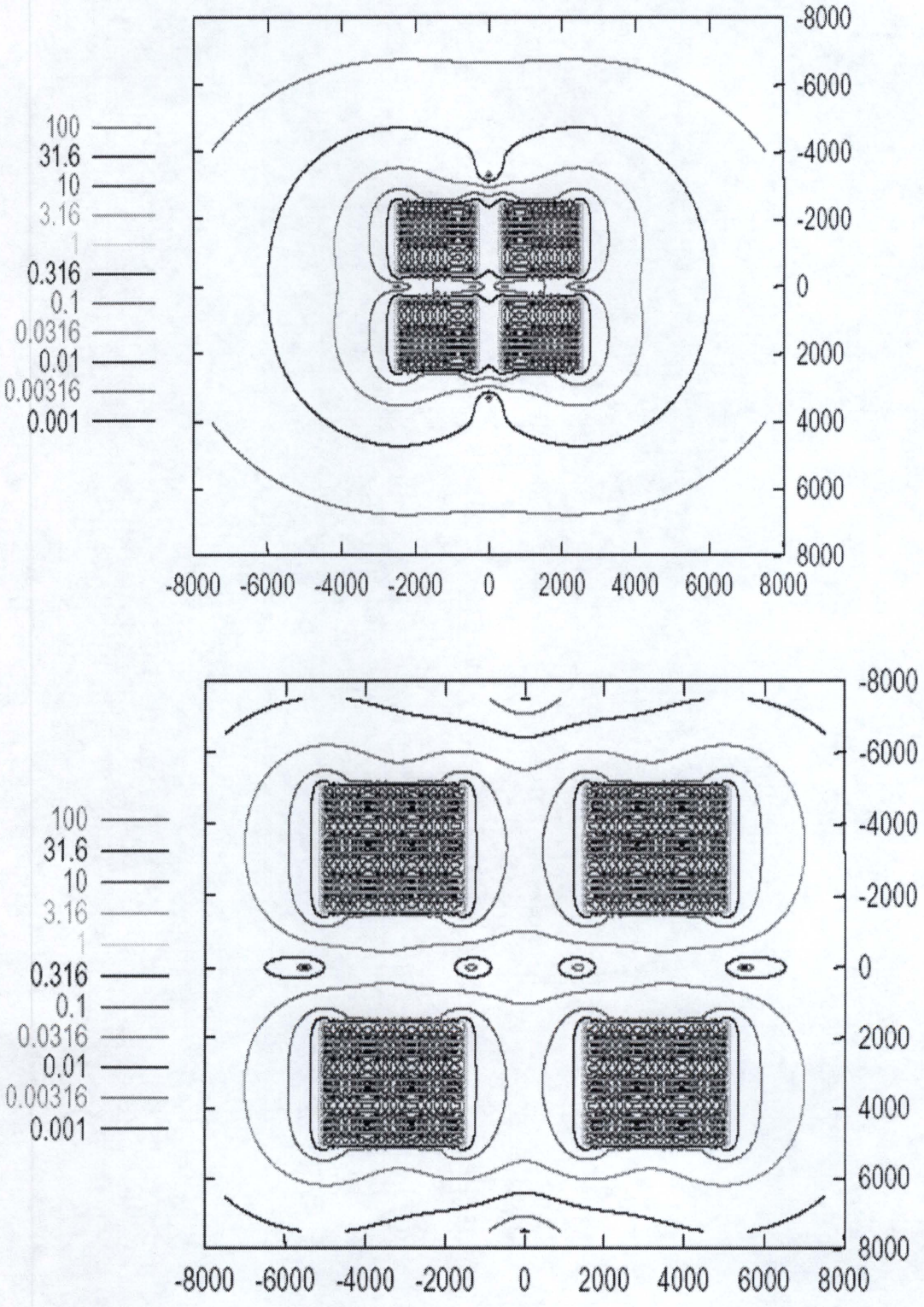


Figure 15. Electric field enhancements in vicinity of 3 different nanoparticle arrays. Distances are in Bohr.

To compare our simulation results to experimental results, we needed to develop a scheme to average electric field enhancements in the vicinity of our nanoparticle arrays. We have defined a 'pocket' within which we compute average observed enhancement. This pocket is defined as all empty space within the nanoparticle array plus all area included within one half the interfacial distance outside of the array. Figure 15 depicts nanoparticle dipole element locations and probe point locations within the sampling pocket.

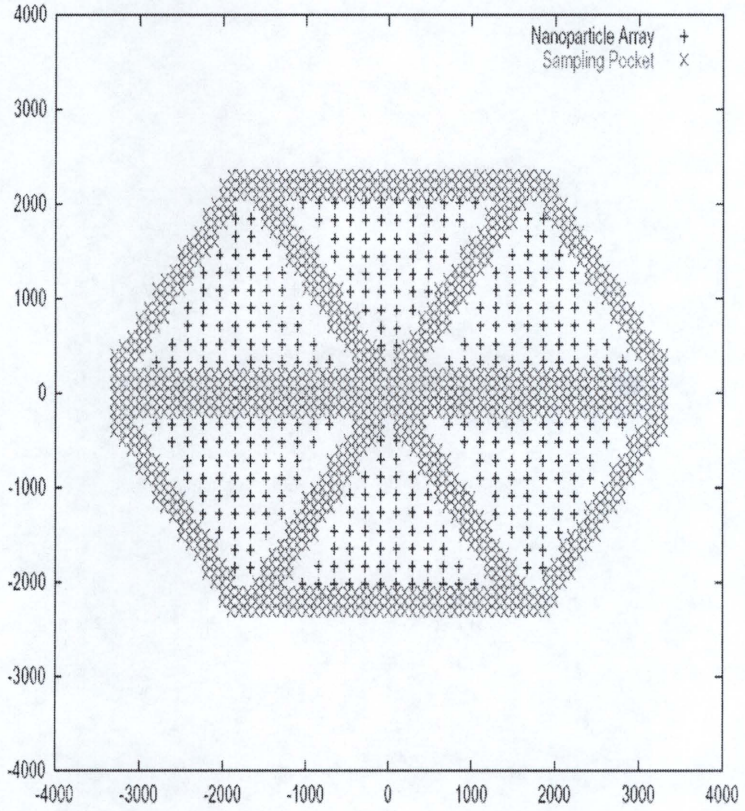

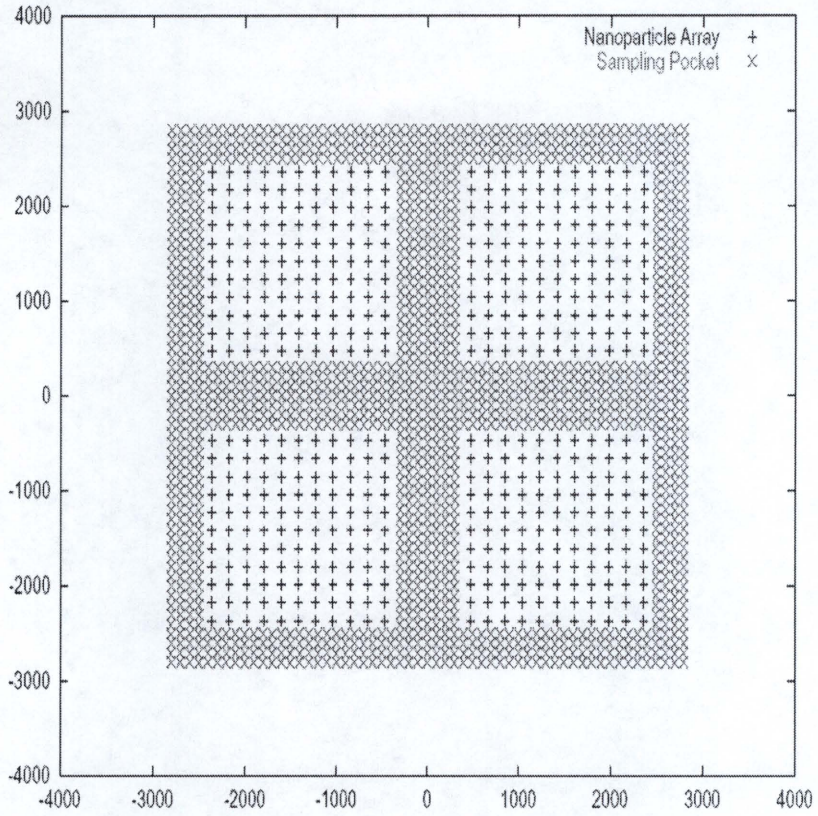
Nanoparticle Array +
Sampling Pocket x
4000
3000
2000
1000
0
-1000
-2000
-3000
-4000
-4000 -3000 -2000 -1000 0 1000 2000 3000 4000

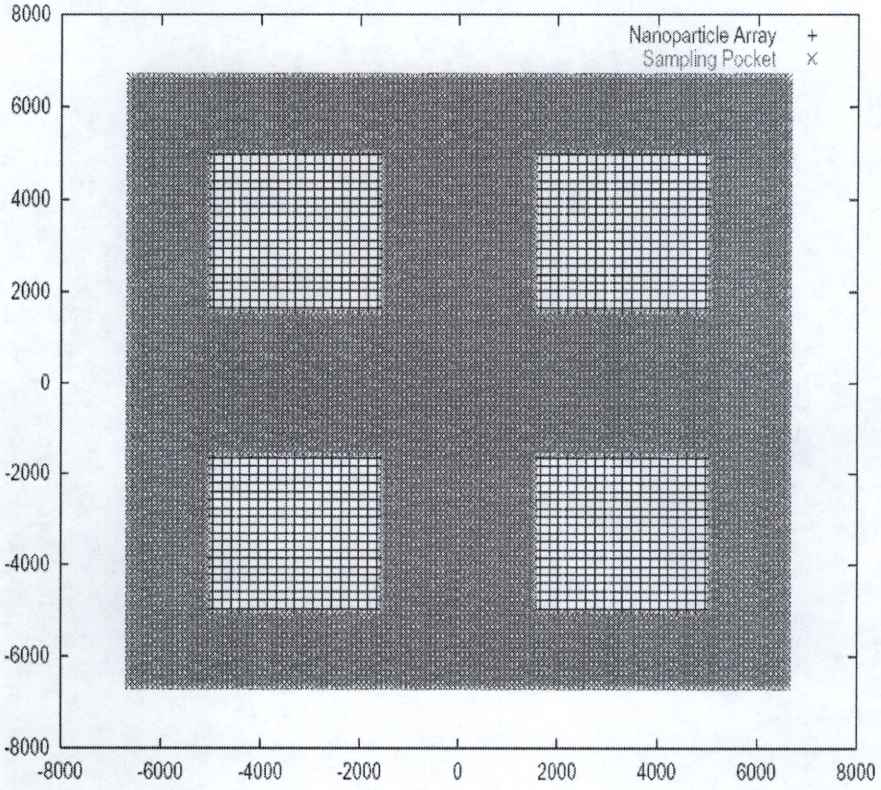
Nanoparticle Array +
Sampling Pocket x
8000
6000
4000
2000
0
-2000
-4000
-6000
-8000
-8000 -6000 -4000 -2000 0 2000 4000 6000 8000

Figure 15. Nanoparticle arrays and sampling pockets for hexamer, quadramer-small, and quadramer-big. All distances are in Bohr.

We have compared our results to experimental data [18]. Table 1 contains the experimentally observed SERS signal, simulated electric field enhancement, simulated total electric field, and the fourth power of this simulated total field. The final column is included because Raman scattering signal is roughly proportional to the fourth power of electric field. All results are normalized to 100.

| | Observed Raman Scattering Signal | Simulated Electric Field Increase | Simulated Total Electric Field | (Total Field)^4 |
|---|---|---|---|---|
| HEXAMER | 100 | 100 | 100 | 100 |
| QUADRAMER-SMALL | 61 | 44.99 | 77.56 | 36.19 |
| QUADRAMER-BIG | 39 | 8.81 | 62.81 | 15.56 |

Table 1. Relative increases in Raman scattering and computationally determined electric field measurements

The most pertinent category in the above table for comparing simulation results to experimental observations is the fourth power measurement. We observe that the qualitative trend in increase in SERS signal is reproducible via DDA calculations. Quantitatively, our results bear some resemblance to experiment. The observed qualitative trend is easily justified with simple arguments. The worst scattering signal is observed in the array called quadramer-big. The nanoparticles in this array are simply too large and too far apart to effectively 'communicate' with each other and produce large increases in electric field, leading to associated increases in Raman scattering. Better signal is observed for the quadramer-small array. Nanoparticles here are of the appropriate size and separation for Raman scattering. The hexamer arrangement yields the greatest Raman scattering signal. We believe that, in addition to having appropriate dimensionality for SERS, this array introduces a certain degree of asymmetry that is conducive to Raman scattering. The asymmetry of individual triangles acts to magnify electric field at the tips of triangles. The highly symmetric arrangements of triangles acts to cancel out some of this phenomenon, but the increase in SERS signal is still aparent.

## 4. Conclusion:

We have successfully developed a working code for the discrete-dipole approximation that can simulate the effects of an inhomogenous electric field on very small spheres of arbitrary dielectric constant. For simulations of dirty ice spheres, accurate results have not proven too computationally expensive to achieve. A metal such as silver, though, with a larger imaginary component of the dielectric constant, requires a far greater degree of subdivision and thus more memory and time to reach satisfactory results. Symmetry considerations may significantly reduce the amount of memory required for simulations, but we may lose the ability to adapt the code to arbitrary scenarios, specifically non-symmetric arrangements of nanoparticles.

Electric field magnifications between two silver rectangular prisms have been simulated. For SERS purposes, this two-prism system is not of significant value. What is of value, however, is that we have laid the groundwork to extend our simulation to more elaborate two-nanoparticle systems or, more importantly, networks composed of these shapes. We have successfully compared DDA calculated electric field enhancements with observed relative amounts of Raman scattering for three different arrays of nanoparticles. Now that we have demonstrated the DDA's ability to model simple arrays of nanoparticles, we may develop more elaborate arrays of nanoparticles designed specifically to maximize Raman scattering numerically before stepping into the lab. As electron beam lithography is very expensive, this work may allow researchers to avoid the construction of trial arrays to empirically determine optimal nanoparticle geometries.

**References:**


[1] Purcell, E. M., Pennypacker, C. R., The Astrophysical Journal. 186 (1973) 705-714.
[2] Draine, B. T., The Astrophysical Journal. 333 (1988) 484-872.
[3] Hinde, R. J., Sepaniak, M. J., Compton, R. N., Nordling, J., Lavrik, N., Chem. Phys. Lett. 339 (2001) 167-173.
[4] van de Hulst, H. C., *Light Scattering by Small Particles*. Dover Publications. New York: 1981
[5] Bohren, C. F., Huffman, D. R., *Absorption and Scattering of Light by Small Particles*. Wiley-Interscience. New York: 1983.
[6] Palik, E. D. *Handbook of Optical Constants of Solids*. Academic Press. San Diego: 1998
[7] Matzler, C. Research Report No. 2002-08: MATLAB Functions for Mie Scattering and Absorption. Institute for Applied Physics. Bern, Switzerland. 2002.
[8] Petravic, M., Kuo-Petravic, G., J. Comp. Phys. 32 (1973) 263.
[9] Fleischman, M., Hendra, P. J., McQuillan, A. J., Chem. Phys. Lett. 26 (1974) 123.
[10] Stratton, J.A. *Electromagnetic Theory*. McGraw-Hill: New York, 1941.
[11] Rahmani, A., Chaumet, P.C., Bryant, G.W. 2004, ApJ, 607, 873.
[12] NIST Webbook Online Database. http://webbook.nist.gov
[13] Romanov, N.P., Shuklin, V.S. Optics and Spectroscopy. 38 (1975) 646.
[14] Albrecht, M.G., Creighton, J.A. J. Am. Chem. Soc. 99 (1977) 5215.
[15] Mie G., *"Beiträge zur Optik trüber Medien, speziell kolloidaler Metallösungen"* Ann. Phys. 25, 377-452 (1908)
[16] Jackson, J. D. *Classical Electrodynamics*, 3rd Ed. Wiley. New York, 1998.
[17] Foster, M., Furse, M., Passno, D. Surface Science. 502-503 (2002) 102-108.
[18] DeJesus, M. private communication.